C-terminal splice variants of P/Q-type Ca^{2+} channel $Ca_V2.1$ α_1 subunits are differentially regulated by Rab3-interacting molecule proteins

Received for publication, January 29, 2017, and in revised form, March 26, 2017 Published, Papers in Press, April 4, 2017, DOI 10.1074/jbc.M117.778829

Mitsuru Hirano[‡], Yoshinori Takada[‡], Chee Fah Wong[‡§], Kazuma Yamaguchi[‡], Hiroshi Kotani[‡], Tatsuki Kurokawa[‡], Masayuki X. Mori[‡], Terrance P. Snutch[¶], Michel Ronjat[‖], Michel De Waard[‖], and Yasuo Mori[‡1]**

*From the [‡]Department of Synthetic Chemistry and Biological Chemistry, Graduate School of Engineering, and the **Department of Technology and Ecology, Hall of Global Environmental Studies, Kyoto University, Kyoto 615-8510, Japan, the [§]Department of Biology, Faculty of Science and Mathematics, Universiti Pendidikan Sultan Idris, 35900 Tanjung Malim, Perak, Malaysia, the [¶]Michael Smith Laboratories and Djavad Mowafaghian Centre for Brain Health, University of British Columbia, Vancouver, British Columbia V6T 1Z4, Canada, and the [‖]LabEx Ion Channels, Science and Therapeutics, INSERM UMR1087/CNRS UMR6291, Institut du Thorax, Université de Nantes, Nantes F-44000, France*

Edited by F. Anne Stephenson

Voltage-dependent Ca^{2+} channels (VDCCs) mediate neurotransmitter release controlled by presynaptic proteins such as the scaffolding proteins Rab3-interacting molecules (RIMs). RIMs confer sustained activity and anchoring of synaptic vesicles to the VDCCs. Multiple sites on the VDCC α_1 and β subunits have been reported to mediate the RIMs-VDCC interaction, but their significance is unclear. Because alternative splicing of exons 44 and 47 in the P/Q-type VDCC α_1 subunit $Ca_V2.1$ gene generates major variants of the $Ca_V2.1$ C-terminal region, known for associating with presynaptic proteins, we focused here on the protein regions encoded by these two exons. Co-immunoprecipitation experiments indicated that the C-terminal domain (CTD) encoded by $Ca_V2.1$ exons 40–47 interacts with the α-RIMs, RIM1α and RIM2α, and this interaction was abolished by alternative splicing that deletes the protein regions encoded by exons 44 and 47. Electrophysiological characterization of VDCC currents revealed that the suppressive effect of RIM2α on voltage-dependent inactivation (VDI) was stronger than that of RIM1α for the $Ca_V2.1$ variant containing the region encoded by exons 44 and 47. Importantly, in the $Ca_V2.1$ variant in which exons 44 and 47 were deleted, strong RIM2α-mediated VDI suppression was attenuated to a level comparable with that of RIM1α-mediated VDI suppression, which was unaffected by the exclusion of exons 44 and 47. Studies of deletion mutants of the exon 47 region identified 17 amino acid residues on the C-terminal side of a polyglutamine stretch as being essential for the potentiated VDI suppression characteristic of RIM2α. These results suggest that the interactions of the $Ca_V2.1$ CTD with RIMs enable $Ca_V2.1$ proteins to distinguish α-RIM isoforms in VDI suppression of P/Q-type VDCC currents.

Fine regulation of neurotransmitter release is integral to adaptive functions of the nervous system, including learning, memory, and cognition. Neurotransmitter release is triggered by depolarization-induced Ca^{2+} influx via voltage-dependent Ca^{2+} channels (VDCCs)[2] in presynaptic active zones (AZs), where synaptic vesicles (SVs) dock in close vicinity to VDCCs at the presynaptic membrane (1, 2). Among different VDCC types, which are distinguished on the basis of their pharmacological and biophysical properties, L-, N-, R-, and P/Q-types have been reported to mediate Ca^{2+} influx responsible for neurotransmitter release (3–6). Different VDCC types show distinct tissue expression patterns, subcellular localizations, activity-dependent properties, and amounts of Ca^{2+} influx, all of which contribute to the fine regulation of neurotransmitter release (7–18). In particular, the local Ca^{2+} concentration ($[Ca^{2+}]_{local}$) and spacing between VDCCs and SVs are tightly regulated by the molecular organization of presynaptic AZs and influence the dynamic properties of neurotransmitter release (2, 9, 18–27). It is also understood that the number of open VDCCs, which determines the $[Ca^{2+}]_{local}$ and release probability of SVs, depends on the efficiency of targeting and availability of VDCCs in the AZ (28). In response to membrane depolarization, VDCCs open to evoke $[Ca^{2+}]_{local}$ rises and simultaneously close via inactivation. This negative feedback reduces the number of VDCCs available and restricts the amplitude of Ca^{2+} influx, which is important for the diversification of Ca^{2+} signaling (29). Inactivation of VDCCs in the presynapse is largely dependent upon the inward Ca^{2+} current magnitude and displays only a weak voltage dependence (13, 30).

In the P/Q-type, VDCCs are composed of the pore-forming α_1 subunit ($Ca_V2.1$) and accessory $\alpha_2\delta$, β, and γ subunits. $Ca_V2.1$ is the most abundantly expressed VDCC α_1 subunit in

This work was supported by Grant-in-aid for Scientific Research (B) 16H05140 from the Japan Society for the Promotion of Science. The authors declare that they have no conflicts of interest with the contents of this article.
This article contains supplemental Fig. S1.
[1] To whom correspondence should be addressed: Laboratory of Molecular Biology, Dept. of Synthetic Chemistry and Biological Chemistry, Graduate School of Engineering, Kyoto University, Kyoto 615-8510, Japan. Tel.: 81-75-383-2761; Fax: 81-75-383-2765; E-mail: mori@sbchem.kyoto-u.ac.jp.

[2] The abbreviations used are: VDCC, voltage-dependent Ca^{2+} channel; VDI, voltage-dependent inactivation; polyQ, polyglutamine; AZ, active zone; SV, synaptic vesicle; AP, action potential; RIM, Rab3 interacting molecule; CTD, C-terminal domain encoded by the exons 40–47 in the $Ca_V2.1$ gene; co-IP, co-immunoprecipitation; IP, immunoprecipitation; WB, Western blotting; *I-V*, current density-voltage; RIM-BP, RIM-binding protein; P*XXP*, proline-rich region; EGFP, enhanced GFP.

the mammalian brain (31), and mutations in the $Ca_V2.1$ gene, *cacna1a*, cause several autosomal-dominant neurological disorders, including familial hemiplegic migraine type 1, episodic ataxia type 2, and spinocerebellar ataxia type 6 (SCA6) (32–34). Multiple functional P/Q-type VDCC variants are generated by alternative splicing of subunit genes (31, 35), different subunit compositions (36), post-translational processing (37), and association with interacting proteins (20, 24, 38, 39). Several types of P/Q-type VDCC complexes can be co-localized in a single neuron and are believed to contribute to the fine-tuning of neuronal processes, such as neurotransmitter release, because formation of each type of $Ca_V2.1$ channel complex is regulated in a different manner (35, 40–42).

Rab3-interacting molecules (RIMs) are multidomain scaffolding proteins expressed in secretory cells (43). Long isoform α-RIMs, including RIM1α and RIM2α, contain an N-terminal zinc finger domain, a central PDZ domain, and two C-terminal domains, C_2A and C_2B. Physiological experiments have shown that α-RIMs are essential for docking and priming of SVs and for recruiting and tethering VDCCs to the presynaptic AZ, thereby regulating VDCC function and short-term plasticity of neurotransmitter release (20, 22, 44–49). We have reported that α-RIMs increase neurotransmitter release by sustaining Ca^{2+} influx through strong inhibition of voltage-dependent inactivation (VDI) of VDCCs and by anchoring vesicles in the vicinity of VDCCs via interaction with VDCC β subunits (Fig. 1*A*) (20). We have also revealed that the RIM C-terminal C_2B domain is essential for RIM-β subunit interaction and inhibition of VDI of VDCCs (20, 39). Mutations in the gene encoding RIMs associated with autism and cone-rod dystrophy, *CORD7*, modify this interaction and/or the regulation of VDCC currents (50, 51). Functional coupling of RIM1α to β subunits of VDCCs is also essential for insulin secretion in non-neuronal cells (52). In addition to the β subunits, the PDZ domain of α-RIMs has been reported to interact with the PDZ-binding motif located at the end of the C terminus of α_1 subunits to modulate localization of P/Q- and N-type VDCC complexes to presynaptic AZs (Fig. 1*A*) (22). Thus, α-RIMs may interact with VDCC complexes through multiple sites of the constituent subunits. However, the significance of multipoint interactions among VDCC α_1 subunits, β subunits, and α-RIMs, as well as functional effects of interactions between α-RIMs and the $Ca_V2.1$ C terminus on VDCC currents, remains unclear.

To quantify the functional significance of multipoint interaction, it is interesting to focus on alternative splicing of exons 44 and 47, because this generates major $Ca_V2.1$ C-terminal splice variants expressed in the human cerebellum (Fig. 1*B* and Table 1). Introns 42–44 are flanked by GT/AG splice-site sequences, and alternative splicing leads to either the inclusion or exclusion of exons 43 and 44 (referred to as (*+43 or −43*) and (*+44 or −44*) in Fig. 1*B*) (53). Insertion of a pentanucleotide GGCAG at the beginning of exon 47 allows in-frame translation of exon 47 to produce a long version of the C terminus (referred to as *47*) in Fig. 1*B*). Otherwise, omission of the GGCAG in transcripts causes a frameshift, leading to stop codon termination near the beginning of exon 47 (referred to as (*Δ47*) in Fig. 1*B*) to generate the human homolog of the rabbit VDCC α_{1A} subunit BI-I (Fig. 1*B*) (31, 34, 53). The 12-amino acid region encoded by exon 44 starts with the arginine residue, which is located 292 amino acids downstream from the transmembrane segment S6 of repeat IV. The exon 44-encoded region is thought to have an AT-hook domain, which is a tripartite DNA-binding motif specific for AT-rich sequences that is typically found in nuclear proteins and DNA-binding proteins (54, 55). The 244-amino acid region encoded by exon 47 with the GGCAG insertion starts with the glycine residue, which is located 451 amino acids downstream from S6 of repeat IV. The exon 47-encoded region has Src homology 3 and PDZ domain-binding motifs, which are targets of synaptic proteins such as CASK, Mint1, RIM-binding protein (RIM-BP), and α-RIMs (19, 22, 56). It is also known that expansion of the polyglutamine tract (polyQ), encoded by CAG trinucleotide repeats in exon 47 of human $Ca_V2.1$, causes the neurological disease, SCA6 (34).

Here, we studied the interactions between α-RIMs and the $Ca_V2.1$ C-terminal regions encoded by exons 44 and 47. We revealed the functional impacts of α-RIM interaction with different $Ca_V2.1$ C-terminal regions on its VDI. The 17 amino acid residues on the C-terminal side of the polyQ stretch play an essential role in the pronounced VDI suppression characteristic of RIM2α. In the $Ca_V2.1$ splice variant lacking exons 44 and 47, VDI suppression remained intact for RIM1α, but for RIM2α, it was reduced to a level comparable with that of RIM1α. These results suggest that the CTD region plays an important role in the α-RIM isoform-dependent potentiation of VDI suppression. Also, our data reveal that the interaction of α-RIMs with the CTD regions encoded by exons 44 and 47 is not essential for the suppressive effects of α-RIMs on VDI, further raising the possibility that interactions of the VDCC β subunits with α-RIMs underlie their strong suppressive effects on the VDI of VDCCs.

Results

Characterization of $Ca_V2.1$ C-terminal splice variation in the human cerebellum

We have previously demonstrated that the RIM C-terminal region containing the C_2B domain interacts with VDCC β subunits (20, 39, 50). It has also been reported that PDZ domains of α-RIMs interact with the PDZ-binding motif located at the C-terminal end of $Ca_V2.1$ and $Ca_V2.2$ (Fig. 1*A*) (22, 57). The C-terminal region is highly divergent in VDCC α_1 subunits because of multiple alternative splice sites (58). In particular, splicing out exon 47 generates $Ca_V2.1$ splice variants that lack the most C-terminal region, including the PDZ-binding motif. It is important to quantitatively assess the relative significance of α-RIM interactions with the C-terminal region of $Ca_V2.1$ and the VDCC β subunit by comparing α-RIM actions on P/Q-type VDCCs containing different $Ca_V2.1$ splice variants carrying the C terminus with and without the α-RIM-interacting region. Previous studies have revealed that exons 43, 44, and 47 contribute to C-terminal splice variations in human $Ca_V2.1$ (53), but relative levels of splice variants with different combinations of these exons have not been quantified. We performed sequence analysis of PCR products from a cDNA library of the human cerebellum, in which abundant expressions of α-RIMs and $Ca_V2.1$ mRNAs were reported (39, 59, 60). A set of PCR oligonucleotide primers were located in exon 42 (forward) and

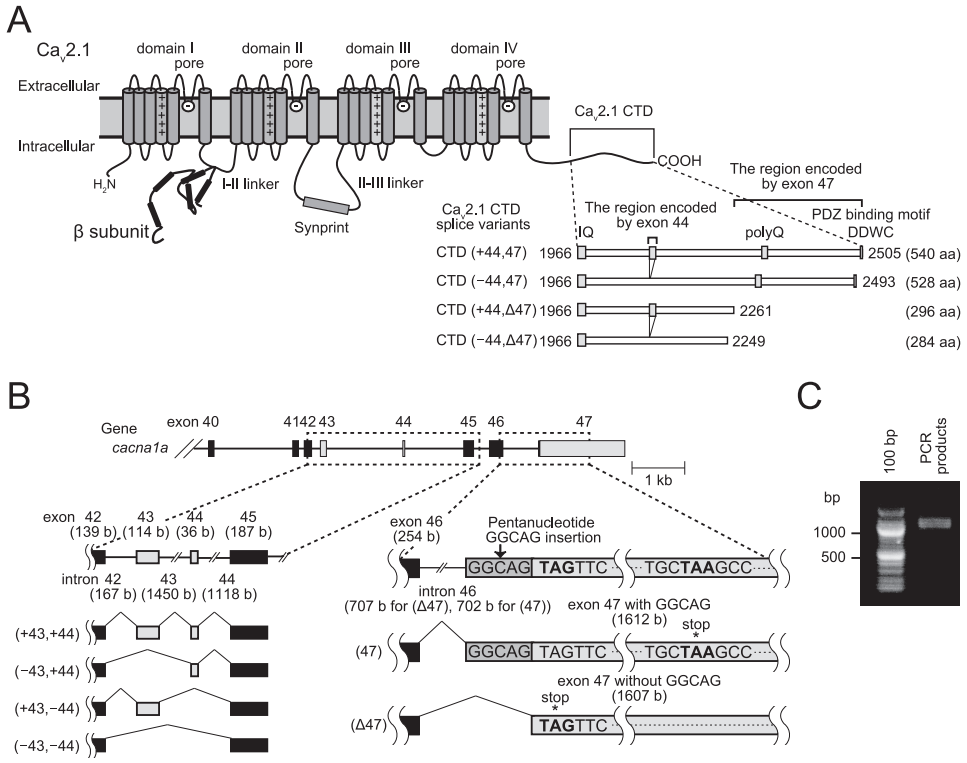

Figure 1. Characterization of splice variants of the $Ca_V2.1$ C terminus in the human cerebellum. *A*, schematic topology of VDCC $Ca_V2.1$ α_1 subunit and β subunit and domain structures of $Ca_V2.1$ CTD splice variants. PolyQ is 11 glutamine (Q) repeats in the cDNA construct subjected to functional characterization. GenBank™ accession numbers are as follows: U79666 for $Ca_V2.1$ CTD (+44,47) and NM_001127221 for $Ca_V2.1$ CTD (+44,Δ47). The exon 44-coding region (GenBank™ accession number Z80152) is eliminated in $Ca_V2.1$ CTD (−44,47) and $Ca_V2.1$ CTD (−44,Δ47). The GGCAG sequence at the 5′-end of exon 47 is eliminated in $Ca_V2.1$ CTD (+44,Δ47) and $Ca_V2.1$ CTD (−44,Δ47). *B, line* represents the structure of the region of the human *cacna1a* gene containing exons 40–47 (*top*), exons 42–45 (*bottom left*), and exons 46 and 47 (*bottom right*). Constitutive exon is shown as *black boxes*, and alternative exon is shown as *gray boxes*. The alternatively spliced sequence GGCAG is indicated by *dark gray boxes*. Stop codons are indicated by *asterisks*. Alternative splicing patterns are indicated by *lines* connecting the exons. *C,* PCR products from human cerebellum cDNA library.

exon 47 (reverse). Agarose gel electrophoresis (1%) revealed a broad band of PCR products of ~1,000 bp consistent with the predicted sizes ranging from 834 to 989 bp (Fig. 1*C*). This DNA band was subcloned into a vector, and the relative levels of splice variants were determined by counting the number of clones containing each exon. The relative proportions of individual splice variants of exon +43/−43, +44/−44, and 47/Δ47 were 100/0, 86/14, and 66/34%, as reported previously (Table 1) (53). $Ca_V2.1$-containing regions encoded by exons 44 and 47 (+44 ,47) were detected at the highest relative proportion (56%) (Fig. 1*A* and Table 1). Relative proportions of $Ca_V2.1$ (+44,Δ47), $Ca_V2.1$ (−44,47), and $Ca_V2.1$ (−44,Δ47) were 30, 11, and 3%, respectively (Fig. 1*A* and Table 1).

Table 1

Characterization of $Ca_V2.1$ C-terminal splice variation in the human cerebellum

n means number of clones sequenced.

Splice variant	% of total	*n*
−43	0	87
+43	100	
−44	14	87
+44	86	
Δ47	34	85
47	66	
+43,+44,47	56	80
+43,−44,47	11	
+43,+44,Δ47	30	
+43,−44,Δ47	3	

Interaction between α-RIMs and $Ca_V2.1$ C-terminal splice variants

We next performed yeast two-hybrid screening of a human brain cDNA library using the C-terminal domain encoded by exons 40–47 of human $Ca_V2.1$, $Ca_V2.1$ CTD (+44,47), as bait, and we identified an interaction between $Ca_V2.1$ CTD and the amino acid residues 487–1349 of human RIM2α (GenBank™ accession number NM_001100117) (Fig. 2*A*). We also performed co-immunoprecipitation (co-IP) experiments to confirm RIM-$Ca_V2.1$ CTD interactions (Fig. 2*B*). As a control, we chose the VDCC β_4 subunit, because β_4 is abundantly expressed in the brain and the spontaneous β_4 mutant lethargic mouse (*cacnb4^{lh}*) has clear neurological defects, supporting the physiological significance of β_4 in the brain (61, 62). YFP-tagged β_4 was co-immunoprecipitated with FLAG-tagged α-RIMs, RIM1α and RIM2α, in HEK293T cells (Fig. 2*C*), as reported previously (20, 39). Next, we performed co-IP between YFP-tagged α-RIMs and FLAG-tagged CTDs of $Ca_V2.1$ variants derived from alternative splicing of exons 44 and 47 in HEK293T cells. RIM1α and RIM2α were co-immunoprecipitated with the $Ca_V2.1$ CTD splice variants except for the variant lacking exons 44 and 47 (Fig. 2*D*). These results suggest that the two regions encoded by exons 44 and 47 contribute significantly to the interaction between the $Ca_V2.1$ CTD and α-RIMs.

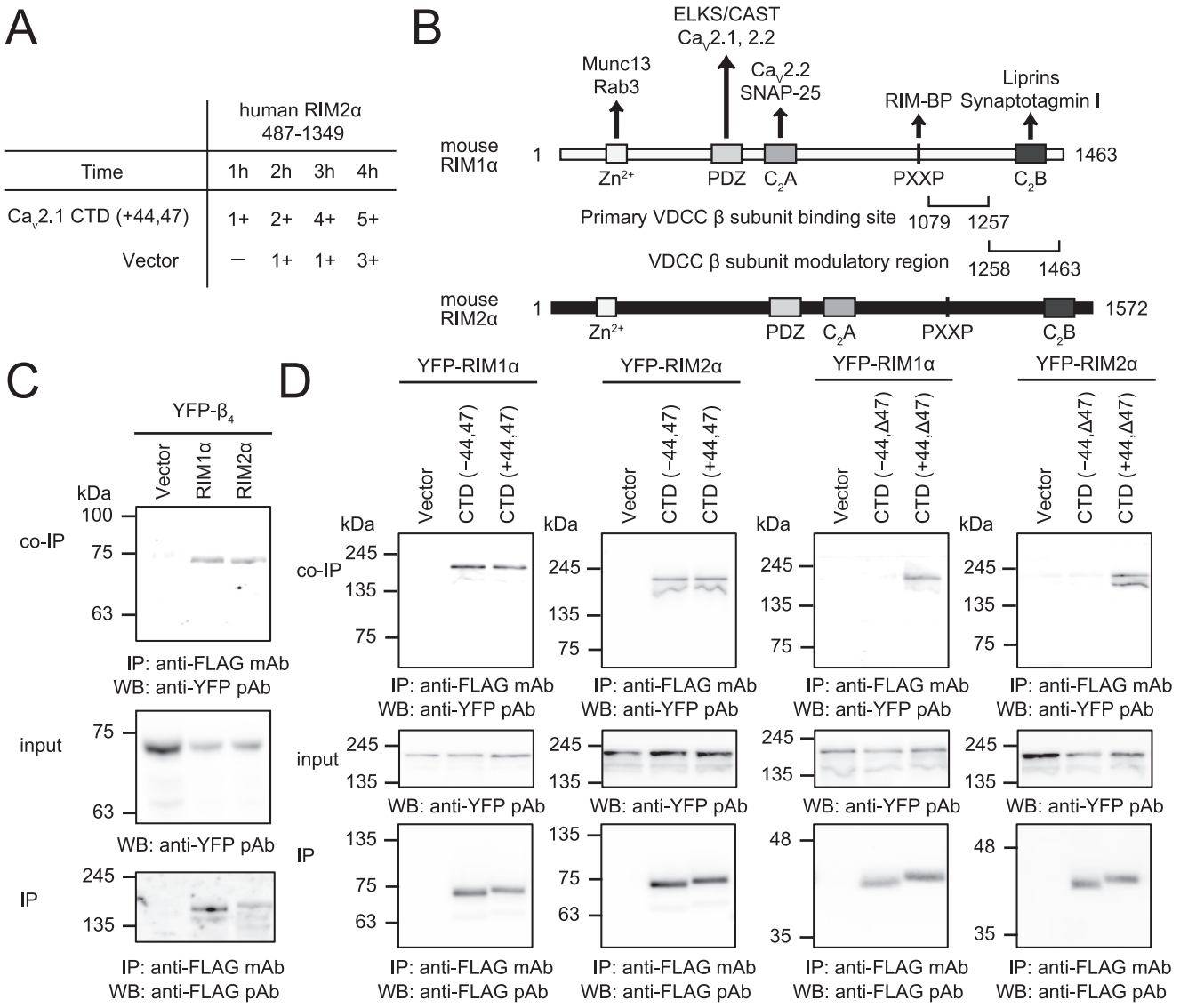

Figure 2. α-RIMs interact with the β_4 subunit and the $Ca_V2.1$ C-terminal splice variants. *A*, yeast two-hybrid results indicating the interaction level of $Ca_V2.1$ CTD (+44,47) with amino acid residues 487–1349 of human RIM2α (GenBank™ accession number NM_001100117.1) as a function of time. The interactions are scored by β-galactosidase activity judged on a scale of one to five, with one meaning "low activity" and five meaning "high activity." *B*, domain structures of mouse α-RIMs. The *arrows* indicate molecules interacting with RIM proteins at the following domains: Zn^{2+} finger-like domain (Zn^{2+}), PDZ domain (PDZ), first and second C_2 domains (C_2A and C_2B), and proline-rich region (*PXXP*). Primary β subunit-binding site (RIM1α(1079–1257)) and β subunit modulatory region (RIM1α(1258–1463)) are indicated (20). *C*, interactions of the YFP-tagged β_4 subunit with FLAG-tagged α-RIMs in HEK293T cells. *D*, interactions of the FLAG-tagged $Ca_V2.1$ CTD splice variants with YFP-tagged α-RIMs in HEK293T cells. The interactions are evaluated by co-IP with monoclonal anti-FLAG antibody, followed by WB with polyclonal anti-YFP antibody. Input is 10% of the amount of cell lysate used for co-IP and is analyzed by WB using polyclonal anti-YFP antibody. Immunoprecipitation (*IP*) of FLAG-tagged $Ca_V2.1$ CTD splice variants or α-RIMs with monoclonal anti-FLAG antibody is analyzed by WB using polyclonal anti-FLAG antibody.

Functional impacts of RIM-$Ca_V2.1$ C-terminal interaction on $Ca_V2.1$ channel properties

We have previously reported that RIMs strongly suppress VDI of neuronal VDCCs by interacting with the β subunits (20, 39, 50). It has also been reported that the RIM-$Ca_V2.1$ C-terminal interaction modulates localization of VDCCs to presynaptic AZs (22). However, the effects of RIM-$Ca_V2.1$ C-terminal interaction on VDCC properties have not been examined. We characterized whole-cell Ba^{2+} currents through recombinant P/Q-type VDCCs containing the $Ca_V2.1$ splice variants, β_4 and $\alpha_2\delta$-1 subunits, in HEK293 cells. We chose Ba^{2+} as a charge carrier, because $Ca_V2.1$ splice variants show different Ca^{2+}-dependent properties in HEK293 cells (63). Voltage dependence of inactivation at different voltages (inactivation curve) (Fig. 3*A*) was first examined in $Ca_V2.1$ (+44,47)-expressing and $Ca_V2.1$ (−44,Δ47)-expressing cells. No significant difference was detected between inactivation curves of $Ca_V2.1$ (+44,47) and $Ca_V2.1$ (−44,Δ47) channels (Fig. 3*B* and Table 2), which is consistent with previous reports (63, 64). In cells co-expressing α-RIMs and $Ca_V2.1$ (−44,Δ47), we detected remarkable inactivation curve shifts toward depolarizing potentials, as described previously (20, 39). Co-expression of RIM2α induced a more significant inactivation curve shift toward depolarizing potentials compared with that for RIM1α in $Ca_V2.1$ (+44,47)-expressing cells, whereas this difference between α-RIMs was not observed in $Ca_V2.1$ (-44,Δ47)-expressing cells (the half-in-

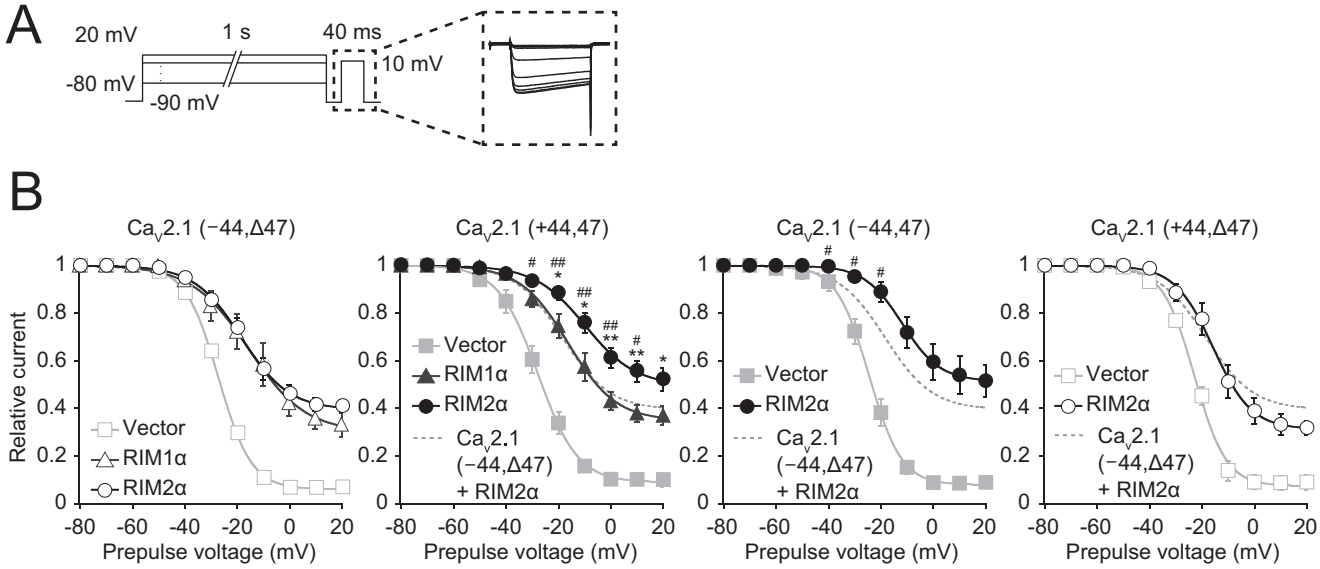

Figure 3. Effects of α-RIMs on VDI of P/Q-type $Ca_V2.1$ channels. *A*, voltage protocol to determine the inactivation curve and representative traces for Ba^{2+} currents. To determine the voltage dependence of inactivation, currents are evoked by a 40-ms test pulse to 10 mV after the 10-ms repolarization to −90 mV following 1-s V_{pre} displacements (conditioning pulses) from −80 to 20 mV with 10-mV increments. *B*, effects of α-RIMs on inactivation curves of Ba^{2+} currents mediated by P/Q-type $Ca_V2.1$ splice variants in HEK293 cells expressing β_4 and $\alpha_2\delta$-1 subunits. The inactivation curve in cells co-expressing RIM2α and $Ca_V2.1$ (−44,Δ47) (*dashed gray line*) is taken from *left panel* and is shown for comparison. *, $p < 0.05$, and **, $p < 0.01$, statistical significance of differences between RIM1α- and RIM2α-expressing cells. #, $p < 0.05$, and ##, $p < 0.01$, statistical significance of differences *versus* cells co-expressing RIM2α and $Ca_V2.1$ (−44,Δ47). See Table 2 for statistical significance of the differences. *Error bars,* S.E.

Table 2

Effect of α-RIMs on inactivation properties of P/Q-type VDCCs in HEK293 cells expressing $Ca_V2.1$s, α_2/δ-1, and β_4

* is $p < 0.05$; ** is $p < 0.01$; ***is $p < 0.001$ *versus* vector. # is $p < 0.05$; ## is $p < 0.01$ *versus* RIM1α. † is $p < 0.05$; †† is $p < 0.01$ *versus* $Ca_V2.1$ (−44,Δ47) for cells co-expressing RIM2α. The number of cells analyzed are indicated in parentheses.

		Inactivation parameters		
		A	$V_{0.5}$	*k*
			mV	*mV*
$Ca_V2.1$ (+44,47)	Vector	0.91 ± 0.02 (5)	−30.0 ± 1.9 (5)	−7.6 ± 0.4 (5)
	RIM1α	0.63 ± 0.04 (11)***	−16.9 ± 2.4 (11)**	−6.6 ± 0.7 (11)
	RIM2α	0.53 ± 0.04 (13)***	−6.7 ± 2.3 (13)***, ##, ††	−9.9 ± 1.0 (13)#
$Ca_V2.1$ (−44,Δ47)	Vector	0.94 ± 0.01 (5)	−27.1 ± 0.6 (5)	−6.2 ± 0.2 (5)
	RIM1α	0.67 ± 0.06 (5)**	−16.2 ± 4.2 (5)*	−8.4 ± 0.9 (5)
	RIM2α	0.61 ± 0.02 (15)***	−17.2 ± 2.1 (15)*	−7.7 ± 0.6 (15)
$Ca_V2.1$ (−44,47)	Vector	0.92 ± 0.03 (5)	−24.8 ± 1.5 (5)	−6.2 ± 1.0 (5)
	RIM2α	0.51 ± 0.07 (7)**	−8.6 ± 2.0 (7)***, †	−8.4 ± 1.1 (7)
$Ca_V2.1$ (+44,Δ47)	Vector	0.92 ± 0.03 (4)	−23.0 ± 0.7 (4)	−6.0 ± 0.2 (4)
	RIM2α	0.69 ± 0.03 (5)**	−15.4 ± 2.4 (5)*	−6.9 ± 1.1 (5)
$Ca_V2.1$ (+44,47) Gln-40	Vector	0.96 ± 0.02 (4)	−30.6 ± 2.0 (4)	−7.1 ± 0.6 (4)
	RIM2α	0.42 ± 0.08 (8)***, ††	−11.0 ± 2.2 (8)***	−8.5 ± 0.8 (8)

activation potentials ($V_{0.5}$) for $Ca_V2.1$ (+44,47) and $Ca_V2.1$ (−44,Δ47) with RIM2α were −6.7 ± 2.3 and −17.2 ± 2.1 mV, respectively) (Fig. 3*B* and Table 2). Considering that the previously reported PDZ domain-binding region is not present in the C-terminal end of $Ca_V2.1$ (−44,Δ47), RIM-β subunit interaction may play major roles in suppressing VDI of VDCCs, whereas RIM-$Ca_V2.1$ C-terminal interaction potentiates this regulatory effect exerted by α-RIMs on VDCCs.

To further assess the importance of interactions via the regions encoded by exons 44 and 47 in this potentiation characteristic of RIM2α in suppression of VDI, we examined the effect of RIM2α on $Ca_V2.1$ (−44,47) and $Ca_V2.1$ (+44,Δ47) inactivation curves. A significantly enhanced shift in the inactivation curve toward depolarizing potentials was detected in cells co-expressing RIM2α and $Ca_V2.1$ (−44,47), but not in cells co-expressing RIM2α and $Ca_V2.1$ (+44,Δ47), compared with cells co-expressing RIM2α and $Ca_V2.1$ (−44,Δ47) ($V_{0.5}$ of $Ca_V2.1$ (−44,47) and $Ca_V2.1$ (+44,Δ47) with RIM2α was −8.6 ± 2.0 and −15.4 ± 2.4 mV, respectively) (Fig. 3*B* and Table 2). We could not observe a significant difference between $Ca_V2.1$ (+44,47) and $Ca_V2.1$ (−44,Δ47) in current density-voltage (*I-V*) relationships, with or without RIM2α co-expression (Fig. 4 and Table 3). These results suggest that the RIM-$Ca_V2.1$ C-terminal interaction via the region encoded by exon 47 is important for the potentiated suppressive effect of RIM2α on VDI.

Inactivation kinetics of P/Q-type VDCCs was characterized by analyzing the decay phase of Ba^{2+} currents evoked by 1-s test pulses in HEK293 cells (Fig. 5*A*). The decay phase was well fitted by two exponential functions with a non-inactivating component (Fig. 5*B*) as reported previously (41). The two exponential time constants (τ_{fast} and τ_{slow}) and the ratio of fast, slow, and non-inactivating components were similar in $Ca_V2.1$ (+44,47)- and $Ca_V2.1$ (−44,Δ47)-expressing cells at test poten-

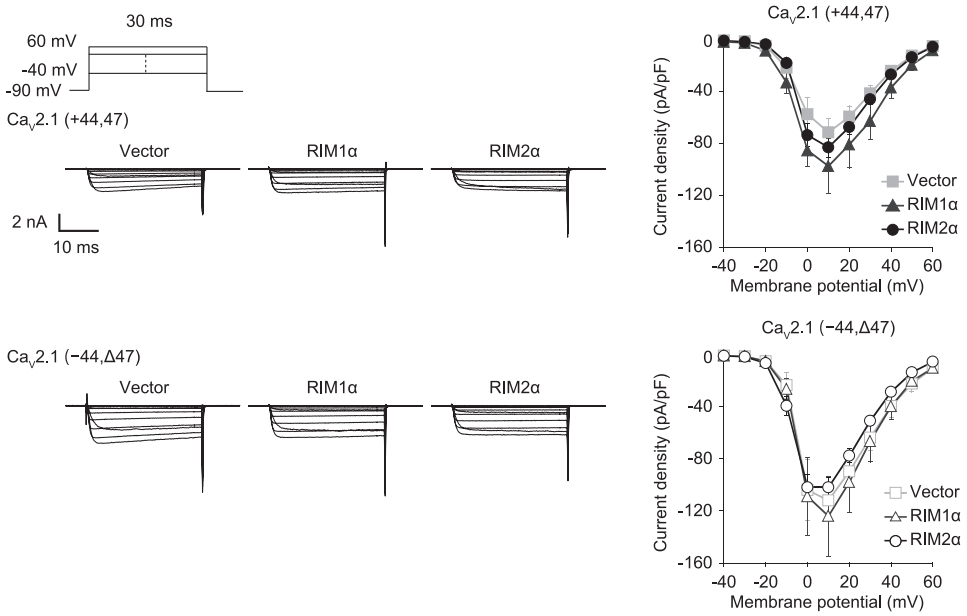

Figure 4. Effects of α-RIMs on the *I-V* relationships of P/Q-type $Ca_V2.1$ channels. *I-V* relationships of $Ca_V2.1$ splice variants in HEK293 cells expressing β_4 and $\alpha_2\delta$-1 subunits. *Left,* representative traces for Ba^{2+} currents on application of test pluses from −40 to 60 mV with 10-mV increments from a holding potential (V_h) of −90 mV. *Right, I-V* relationships of $Ca_V2.1$ splice variants. See Table 3 for statistical significance of the differences. *Error bars,* S.E.

Table 3

Effect of α-RIMs on the *I-V* relationships of P/Q-type VDCCs in HEK293 cells expressing $Ca_V2.1$s, α_2/δ-1, and β_4

The number of cells analyzed are indicated in parentheses.

		Current density[a]	$V_{0.5}$	k
		pA/picofarad	*mV*	*mV*
$Ca_V2.1$ (+44,47)	Vector	−71.7 ± 10.8 (5)	−3.0 ± 1.3 (5)	4.5 ± 0.2 (5)
	RIM1α	−97.5 ± 21.3 (5)	−5.1 ± 1.9 (5)	4.5 ± 0.4 (5)
	RIM2α	−83.1 ± 7.5 (7)	−3.7 ± 1.1 (7)	3.7 ± 0.6 (7)
$Ca_V2.1$ (−44,Δ47)	Vector	−111.5 ± 13.8 (4)	−4.0 ± 1.6 (4)	3.0 ± 0.3 (4)
	RIM1α	−123.8 ± 30.6 (4)	−3.2 ± 1.7 (4)	3.6 ± 0.6 (4)
	RIM2α	−102.5 ± 7.4 (7)	−6.5 ± 1.0 (7)	3.6 ± 0.3 (7)

[a] Ba^{2+} currents evoked by depolarizing pulse to 10 mV from a V_h of −90 mV are divided by capacitance.

tials of 0, 10, and 20 mV (Fig. 5, *C* and *D*, and Table 4). Co-expression of α-RIMs exerted common effects on Ba^{2+} currents in $Ca_V2.1$ (+44,47)- and $Ca_V2.1$ (−44,Δ47)-expressing cells. The fast-inactivating component was significantly decreased at 0 and 10 mV, whereas the non-inactivating component as well as τ_{slow} were significantly increased by α-RIMs at 0, 10, and 20 mV (Fig. 5, *C* and *D*, and Table 4). Thus, it is unlikely that these effects are mediated by interaction of α-RIMs with the $Ca_V2.1$ C-terminal region encoded by exons 44 and 47. In cells co-expressing RIM2α and $Ca_V2.1$ (+44,47), increases in the non-inactivating component at 0, 10, and 20 mV and τ_{fast} at 0 and 10 mV were more pronounced compared with cells co-expressing RIM2α and $Ca_V2.1$ (−44,Δ47) (Fig. 5, *C* and *D*, and Table 4). This effect can be mediated by the RIM2α-$Ca_V2.1$ C-terminal interaction. Furthermore, currents evoked by trains (100 Hz) of action potential (AP)-like waveforms for 3 s, a more physiological voltage-clamp protocol used to determine closed-state inactivation (65), showed a more rapid decrease in amplitude in cells co-expressing RIM2α and $Ca_V2.1$ (−44,Δ47) compared with cells co-expressing RIM2α and $Ca_V2.1$ (+44,47) (Fig. 5*E*). These results suggest that RIM2α-$Ca_V2.1$ C-terminal interaction is not essential for but enhances the VDI suppression induced by α-RIMs.

It is important to note that, without the interaction of α-RIMs, these splice variants were indistinguishable in channel properties such as inactivation curve (Fig. 3 and Table 2), inactivation kinetics (Fig. 5 and Table 4), and *I-V* relationship (Fig. 4 and Table 3). This underscores the significance of protein-protein interaction in differentiating functional properties of alternatively spliced $Ca_V2.1$ variants.

Biochemical characterization of the RIM2α-$Ca_V2.1$ C-terminal interaction

The $Ca_V2.1$ mutant, $Ca_V2.1$ (+44,47) ΔDDWC, which lacks four amino acids (DDWC) in the C-terminal end was constructed, because these four amino acids bind to the PDZ domain of α-RIMs (22, 57). Inactivation curves of whole-cell Ba^{2+} currents in HEK293 cells co-expressing RIM2α and $Ca_V2.1$ (+44,47) ΔDDWC were indistinguishable from those in cells co-expressing RIM2α and $Ca_V2.1$ (+44,47), showing shifts toward depolarizing potentials compared with the inactivation curves in cells co-expressing RIM2α and $Ca_V2.1$ (−44,Δ47) ($V_{0.5}$ of $Ca_V2.1$ (+44,47) ΔDDWC, $Ca_V2.1$ (+44,47), and $Ca_V2.1$ (−44,Δ47) were −6.7 ± 3.2 mV, −6.7 ± 2.3 mV, and −17.2 ± 2.1 mV, respectively) (Fig. 6*A* and Table 5). In co-IP experiments, YFP-tagged RIM2α showed association with FLAG-tagged $Ca_V2.1$ CTD (+44,47) ΔDDWC in HEK293T cells (Fig. 6*B*). The intensity of the co-IP band for RIM2α normalized to the IP band for the CTD was significantly decreased in cells co-expressing RIM2α and $Ca_V2.1$ CTD (+44,47) ΔDDWC, compared with cells co-expressing RIM2α and $Ca_V2.1$ CTD (+44,47) (Fig. 6*C*). These data suggest that DDWC in the region encoded by exon 47 contributes to the RIM2α-$Ca_V2.1$ C-terminal interaction, as reported previously (22, 57), but not to potentiation of VDI suppression by RIM2α.

To clarify the RIM2α-interacting regions responsible for the potentiation of VDI suppression by RIM2α, additional deletion mutants of $Ca_V2.1$ were constructed (Fig. 7*A*). In cells

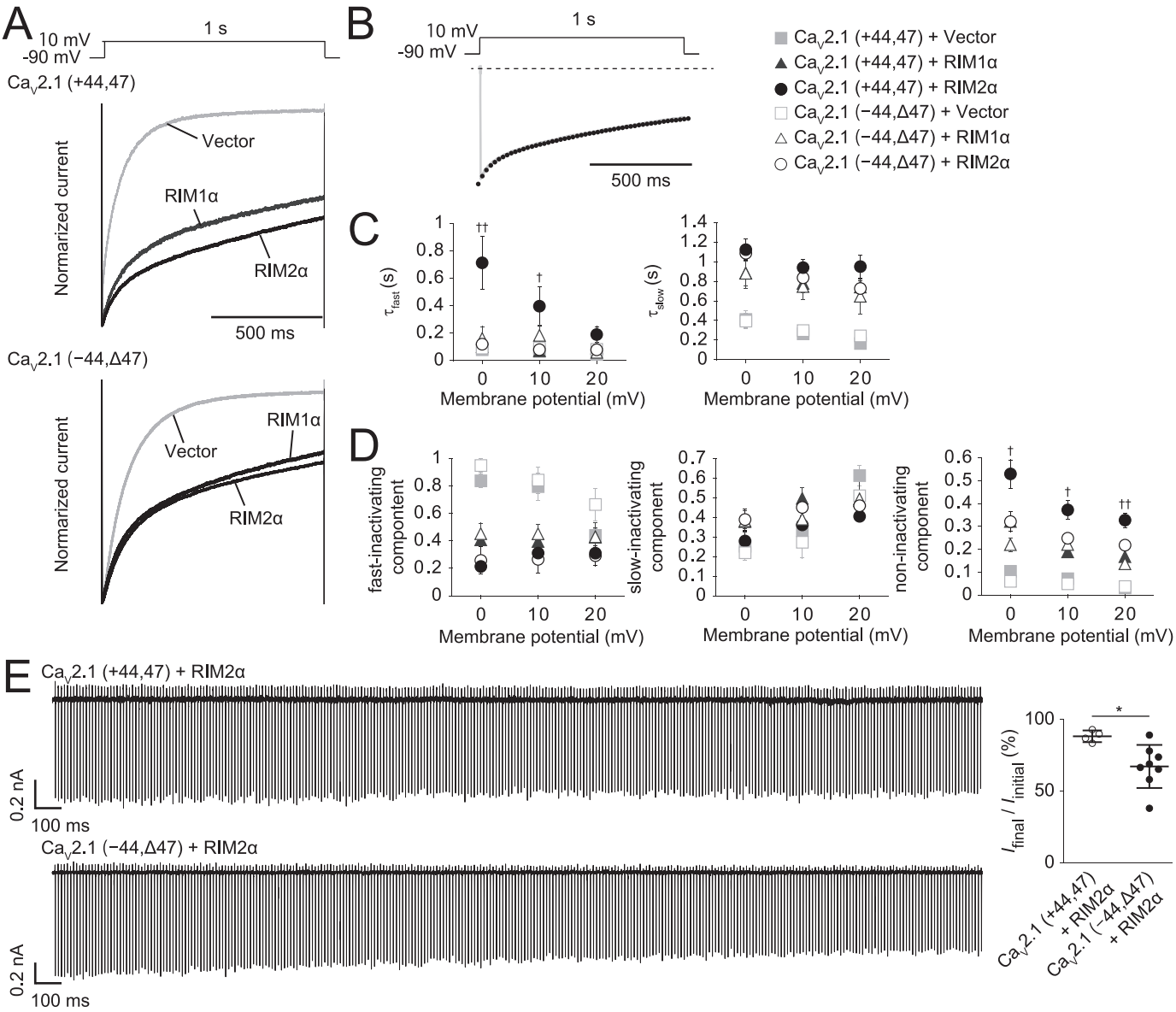

Figure 5. Effects of α-RIMs on VDI kinetics of P/Q-type $Ca_V2.1$ channels. *A,* effects of α-RIMs on inactivation of Ba^{2+} currents mediated by P/Q-type $Ca_V2.1$ splice variants in HEK293 cells expressing β_4 and $\alpha_2\delta$-1 subunits. The peak amplitudes are normalized for Ba^{2+} currents elicited by 1-s pulses to 10 mV from a V_h of −90 mV. *B,* Ba^{2+} current evoked by 1-s test pulse to 10 mV from a V_h of −90 mV in HEK293 cells expressing β_4, $\alpha_2\delta$-1 subunits, and RIM1α. Current decay is fitted by a sum of two exponential functions with time constants of 55 and 995 ms, whose fraction of components is 0.19 and 0.61, respectively. The fraction of its non-inactivating component is 0.24. *C,* voltage dependence of the two inactivation time constants, τ_{fast} and τ_{slow}. The mean inactivation time constants are plotted as a function of test potential from 0 to 20 mV. *D,* voltage dependence of the fraction of the three components, fast-, slow-, and non-inactivating components. The fractions of the components are plotted against test potentials. †, $p < 0.05$; ††, $p < 0.01$; statistical significance of differences between cells co-expressing $Ca_V2.1$ (−44,Δ47) and RIM2α and cells co-expressing $Ca_V2.1$ (+44,47) and RIM2α. See Table 4 for statistical significance of the differences. *Error bars,* S.E. *E, left,* effects of RIM2α on Ba^{2+} currents mediated by P/Q-type $Ca_V2.1$ splice variants in response to 100 Hz AP-like voltage command for 3 s in HEK293 cells expressing β_4 and $\alpha_2\delta$-1 subunits (AP-like waveform, −80 to 33 mV; rise time, 0.4 ms; decay time, 1.1 ms). *Right,* percentage of currents in response to the last stimulus compared with currents in response to the first stimulus ($Ca_V2.1$ (+44,47) RIM2α, 88 ± 4%, $n = 4$; $Ca_V2.1$ (−44,Δ47) RIM2α, 67 ± 15%, $n = 8$). Data are presented in scatter plots. The *vertical error bars* represent standard deviations, and the mean values are indicated with *horizontal bars*. *, $p < 0.05$; statistical significance of difference between cells co-expressing $Ca_V2.1$ (−44,Δ47) and RIM2α and cells co-expressing $Ca_V2.1$ (+44,47) and RIM2α.

co-expressing RIM2α with $Ca_V2.1$ (+44,2364X) or $Ca_V2.1$ (+44,2344X), in which C-terminal residues 2365–2505 or 2345–2505 were deleted, respectively, the inactivation curves were similar to those in cells co-expressing RIM2α with $Ca_V2.1$ (+44,47). In contrast, in cells co-expressing RIM2α with $Ca_V2.1$ (+44,2327X) or $Ca_V2.1$ (+44,2313X), in which C-terminal residues 2328–2505 or 2314–2505 were deleted, respectively, the inactivation curves were similar to those in cells co-expressing RIM2α and $Ca_V2.1$ (−44,Δ47) (Fig. 7*B* and Table 5). These data suggest that 17 amino acid residues, 2328–2344 (RPGRAATSGPRRYPGPT), on the C-terminal side of the polyQ stretch of $Ca_V2.1$ (+44,47) is a RIM2α-interacting region that potentiates the suppressive effect on VDI.

In co-IP experiments, however, YFP-tagged RIM2α showed a comparable level of co-IP with FLAG-tagged CTD of $Ca_V2.1$ (+44,2344X) and FLAG-tagged CTD of $Ca_V2.1$ (+44,2327X) but a decreased level of co-IP with CTD of $Ca_V2.1$ (+44,2275X) (Fig. 7*C*). To eliminate possible contributions of exon 44-en-

Table 4

Effect of α-RIMs on inactivation kinetics of P/Q-type VDCCs in HEK293 cells expressing $Ca_V2.1$s, α_2/δ-1, and β_4

* is $p < 0.05$; ** is $p < 0.01$; *** is $p < 0.001$ *versus* vector. # is $p < 0.05$; ## is $p < 0.01$ *versus* RIM1α. † is $p < 0.05$; †† is $p < 0.01$ *versus* $Ca_V2.1$ (−44,Δ47) for cells co-expressing RIM2α. The number of cells analyzed are indicated in parentheses.

			Fraction of components			Time constants	
		mV	Fast	Slow	Sustained	τ_{fast}	τ_{slow}
CaV2.1 (+44,47)	Vector (8)	0	0.84 ± 0.05	0.25 ± 0.05	0.10 ± 0.02	0.08 ± 0.01	0.41 ± 0.09
		10	0.79 ± 0.10	0.33 ± 0.06	0.07 ± 0.01	0.07 ± 0.01	0.26 ± 0.05
		20	0.44 ± 0.05	0.61 ± 0.05	0.03 ± 0.01	0.04 ± 0.01	0.16 ± 0.02
	RIM1α (11)	0	0.41 ± 0.04***	0.38 ± 0.03	0.32 ± 0.02***	0.10 ± 0.04	0.88 ± 0.13*
		10	0.39 ± 0.06**	0.50 ± 0.06	0.19 ± 0.02**	0.07 ± 0.02	0.78 ± 0.09***
		20	0.42 ± 0.07	0.48 ± 0.04	0.17 ± 0.03**	0.09 ± 0.03	0.74 ± 0.09***
	RIM2α (11)	0	0.20 ± 0.03***, ##	0.28 ± 0.05	0.53 ± 0.06***, ##, †	0.71 ± 0.19*, ##, ††	1.12 ± 0.11***
		10	0.30 ± 0.04***	0.36 ± 0.04	0.37 ± 0.04***, ##, †	0.40 ± 0.14#, †	0.94 ± 0.08***
		20	0.30 ± 0.04	0.40 ± 0.02***	0.33 ± 0.03***, ##, ††	0.19 ± 0.06	0.95 ± 0.12***
CaV2.1 (−44,Δ47)	Vector (5)	0	0.95 ± 0.05	0.22 ± 0.04	0.06 ± 0.01	0.09 ± 0.01	0.39 ± 0.08
		10	0.84 ± 0.10	0.27 ± 0.08	0.05 ± 0.01	0.09 ± 0.01	0.29 ± 0.04
		20	0.66 ± 0.12	0.51 ± 0.08	0.04 ± 0.01	0.08 ± 0.01	0.24 ± 0.05
	RIM1α (5)	0	0.45 ± 0.08***	0.38 ± 0.05	0.22 ± 0.03***	0.16 ± 0.08	0.88 ± 0.15*
		10	0.45 ± 0.07*	0.39 ± 0.05	0.22 ± 0.04**	0.18 ± 0.08	0.74 ± 0.13*
		20	0.43 ± 0.10	0.49 ± 0.11	0.14 ± 0.01***	0.06 ± 0.01	0.64 ± 0.18*
	RIM2α (13)	0	0.26 ± 0.10***	0.39 ± 0.05	0.32 ± 0.04**	0.12 ± 0.03	1.08 ± 0.07***
		10	0.26 ± 0.10**	0.45 ± 0.04*	0.25 ± 0.02***	0.08 ± 0.01#	0.83 ± 0.05***
		20	0.29 ± 0.07*	0.46 ± 0.04	0.22 ± 0.02***, #	0.08 ± 0.01	0.72 ± 0.09**

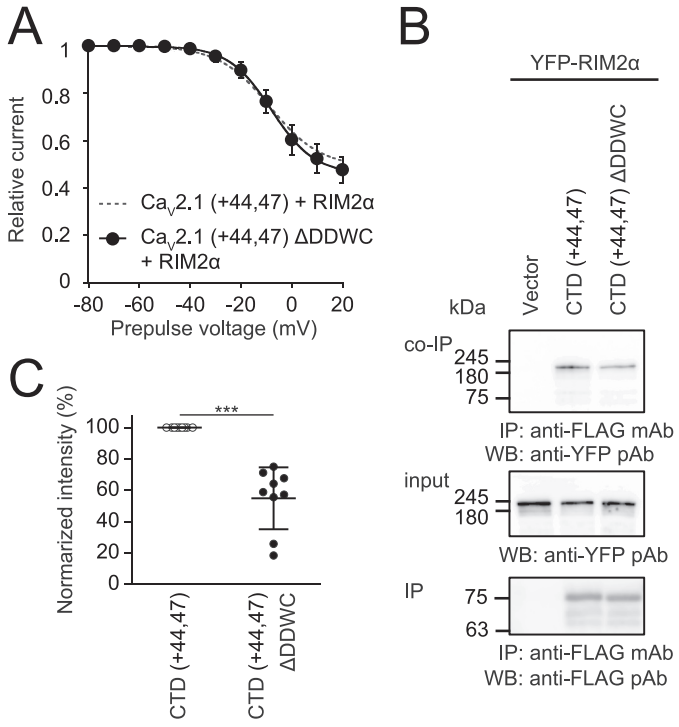

Figure 6. Effects of RIM2α on VDI of the P/Q-type $Ca_V2.1$ deletion mutant lacking DDWC. *A,* effects of RIM2α on inactivation curves of Ba^{2+} currents mediated by P/Q-type $Ca_V2.1$ (+44,47) ΔDDWC, which lacks DDWC at the C-terminal end of $Ca_V2.1$ (+44,47), in HEK293 cells expressing β_4 and $\alpha_2\delta$-1 subunits. The inactivation curve in cells co-expressing RIM2α and $Ca_V2.1$ (+44,47) (*dashed dark gray line*) is taken from Fig. 3 and is shown for comparison. See Table 5 for statistical significance of the differences. *Error bars,* S.E. *B,* interaction of FLAG-tagged $Ca_V2.1$ CTD (+44,47) or $Ca_V2.1$ CTD (+44,47) ΔDDWC with YFP-tagged RIM2α in HEK293T cells. The interactions are evaluated by co-IP with monoclonal anti-FLAG antibody, followed by WB with polyclonal anti-YFP antibody. Input is 10% of the amount of cell lysate used for co-IP and is analyzed by WB using polyclonal anti-YFP antibody. IP of FLAG-tagged $Ca_V2.1$ CTDs with monoclonal anti-FLAG antibody is analyzed by WB using polyclonal anti-FLAG antibody. *C,* quantification of the data shown in *B*. The intensity of the co-IP band for RIM2α normalized to the IP band for the CTD ($Ca_V2.1$ CTD (+44,47), 100%; $Ca_V2.1$ CTD (+44,47) ΔDDWC, 55 ± 20%) (92). Data for nine experiments are presented in scatter plots. The *vertical error bars* represent standard deviations, and the mean values are indicated with *horizontal bars*. ***, $p < 0.001$; statistical significance of difference between CTD (+44,47) and CTD (+44,47) ΔDDWC.

coded amino acid residues to the interaction of RIM2α with CTD mutants, we next constructed deletion mutants of the CTD of $Ca_V2.1$ (−44,47). The co-IP was nearly abolished for the CTD of $Ca_V2.1$ (−44,2263X), in which 2263X corresponds to 2275X in $Ca_V2.1$ (+44,47) (Fig. 7*D*). This result suggests that the amino acid residues 2264–2280 (GTSTPRRGRRQ-LPQTPS) of $Ca_V2.1$ (−44,47), which correspond to 2276–2292 of $Ca_V2.1$ (+44,47), are an important region for the RIM2α-$Ca_V2.1$ CTD interaction. However, the co-IP experiments failed to unveil interaction between the 17 amino acid residues, 2328–2344, of $Ca_V2.1$ (+44,47) with RIM2α, although this region is supposed to be essential for potentiated VDI suppression by RIM2α.

To demonstrate interaction of the 2328–2344 amino acid residues, contributions of the exon 44 region and residues 2276–2292 of $Ca_V2.1$ (+44,47) were eliminated in deletion mutants based upon $Ca_V2.1$ (−44,Δ2264–2280). The level of co-IP was markedly diminished for the CTD of $Ca_V2.1$ (−44,Δ2264–2280,2315X) and $Ca_V2.1$ (−44,Δ2264–2280, 2301X) compared with the CTD of $Ca_V2.1$ (−44,Δ2264–2280,2332X) and $Ca_V2.1$ (−44,Δ2264–2280,2352X) (Fig. 7*E*). This result suggests that the 17 amino acid residues, 2316–2332, of $Ca_V2.1$ (−44,47), which correspond to 2328–2344 of $Ca_V2.1$ (+44,47), indeed constitute an important binding region for RIM2α to exert a potentiated suppressive effect on VDI.

It is interesting to note that deletion of the region encoded by exon 44 failed to elicit suppression of interaction of the $Ca_V2.1$ CTD containing the region encoded by exon 47 (compare the bands of $Ca_V2.1$ CTD (−44,47) and $Ca_V2.1$ CTD (+44,47) in Fig. 2*D*). In contrast, deletion of the region encoded by exon 47 suppressed the interaction of the $Ca_V2.1$ CTD containing the region encoded by exon 44 (compare the bands of $Ca_V2.1$ CTD (+44,Δ47) and $Ca_V2.1$ (+44,47) in Fig. 7*C*). These results suggest that the region encoded by exon 47 binds more strongly to α-RIMs compared with the region encoded by exon 44. Thus, formation of RIM2α-$Ca_V2.1$ complexes is mediated by multipoint interaction.

Table 5

Effects of chimeric RIM and RIM2α deletion mutant on inactivation properties of P/Q-type VDCCs in HEK293 cells expressing $Ca_V2.1$, α_2/δ-1, and β_4

* is $p < 0.05$; ** is $p < 0.01$; *** is $p < 0.001$ *versus* $Ca_V2.1$ (−44,Δ47) for cells co-expressing RIM2α. #, $p < 0.05$ *versus* $Ca_V2.1$ (−44,Δ47) for cells co-expressing RIM1–2 chimera. †, $p < 0.05$ *versus* $Ca_V2.1$ (−44,Δ47) for cells co-expressing RIM2(1183–1572). The number of cells analyzed are indicated in parentheses.

		Inactivation parameters		
		a	$V_{0.5}$	*k*
			mV	*mV*
CaV2.1 (+44,47)	RIM2α	0.53 ± 0.04 (13)	−6.7 ± 2.3 (13)**	−9.9 ± 1.0 (13)
CaV2.1 (−44,Δ47)	RIM2α	0.61 ± 0.02 (15)	−17.2 ± 2.1 (15)	−7.7 ± 0.6 (15)
CaV2.1 (+44,47) ΔDDWC	RIM2α	0.55 ± 0.05 (7)	−6.7 ± 3.2 (7)*	−7.2 ± 1.1 (7)
CaV2.1 (+44,47) 2366X	RIM2α	0.53 ± 0.07 (6)	−6.3 ± 2.3 (6)**	−5.7 ± 0.7 (6)
CaV2.1 (+44,47) 2344X	RIM2α	0.54 ± 0.04 (6)	−8.3 ± 3.0 (6)*	−8.2 ± 0.9 (6)
CaV2.1 (+44,47) 2327X	RIM2α	0.70 ± 0.03 (6)	−14.1 ± 2.4 (6)	−8.4 ± 0.9 (6)
CaV2.1 (+44,47) 2315X	RIM2α	0.67 ± 0.04 (8)	−13.5 ± 1.2 (8)	−6.8 ± 0.5 (8)
CaV2.1 (+44,47)	RIM1–2 chimera	0.49 ± 0.07 (7)	−4.7 ± 2.6 (7)**, #	−8.3 ± 0.7 (7)
	RIM2α (1183–1572)	0.43 ± 0.06 (7)**, ††	−1.9 ± 3.2 (7)***, †	−5.3 ± 1.2 (7)
CaV2.1 (−44,Δ47)	RIM1–2 chimera	0.59 ± 0.03 (3)	−15.9 ± 3.3 (3)	−7.6 ± 1.5 (3)
	RIM2α (1183–1572)	0.69 ± 0.04 (6)	−14.2 ± 4.0 (6)	−7.0 ± 1.4 (6)

Characterization of the RIM2α region responsible for interaction with the $Ca_V2.1$ C terminus

To identify the region in RIM2α that interacts with the $Ca_V2.1$ C terminus, we constructed the chimeric RIM, RIM1–2 chimera, with amino acid residues from the N terminus to the C_2A domain of RIM1α and from the C_2A domain of RIM2α (Fig. 8*A*). We examined effects of the RIM1–2 chimera on whole-cell Ba^{2+} currents mediated by $Ca_V2.1$ (+44,47)- and $Ca_V2.1$ (−44,Δ47)-containing VDCCs (Fig. 8*B*). Significant enhancement of inactivation curve shift by the RIM1–2 chimera toward depolarizing potentials was observed for $Ca_V2.1$ (+44,47) compared with $Ca_V2.1$ (−44,Δ47) ($V_{0.5}$ for $Ca_V2.1$ (+44,47) and $Ca_V2.1$ (−44,Δ47) with RIM1–2 chimera was −4.7 ± 2.6 and −15.9 ± 3.3 mV, respectively) (Fig. 8*B* and Table 5). This tendency of the RIM1–2 chimera suggests that the region on the C-terminal side of the C_2A domain is important for potentiating the suppressive effect of RIM2α on VDI. We also tested a mutant of RIM2α(1183–1572) composed of the amino acid residues 1183–1572 of RIM2α corresponding to the β subunit-binding region in RIM1α (residues 1079–1463 of RIM1α) (Figs. 2*B* and 8*A*) (20, 39). In cells co-expressing RIM2α(1183–1572) and $Ca_V2.1$ (+44,47), we also detected potentiation of the suppressive effect on VDI as observed in cells co-expressing RIM2α(1183–1572) and $Ca_V2.1$ (−44,Δ47) ($V_{0.5}$ and the rates of the inactivating component were −1.9 ± 3.2 mV and 0.43 ± 0.06, respectively, for $Ca_V2.1$ (+44,47) with RIM2α(1183–1572) and 14.2 ± 4.0 mV and 0.69 ± 0.04, respectively, for $Ca_V2.1$ (−44,Δ47) with RIM2α(1183–1572)) (Fig. 8*C* and Table 5). Associations between YFP-tagged RIM2α(1183–1572) and FLAG-tagged mutants based upon $Ca_V2.1$ CTD (−44,Δ2264–2280), which has a deletion of the region corresponding to 2328–2344 of $Ca_V2.1$ (+44,47), were tested by co-IP experiments. RIM2α(1183–1572) showed co-IP with the CTD of $Ca_V2.1$ (−44,Δ2264–2280, 2332X) but not with the CTD of $Ca_V2.1$ (−44,Δ2264–2280, 2315X) or $Ca_V2.1$ (−44,Δ2264–2280, 2301X) (Fig. 8*D*). These data suggest that the C-terminal region containing the C_2B domain is critical for RIM2α to potentiate suppression of VDI and binds with 2328–2344 of $Ca_V2.1$ (+44,47) in addition to the β subunits (20, 39).

Effects of polyQ elongation in the $Ca_V2.1$ C-terminal region on regulation of VDI by RIM2α

The polyQ stretch is an interesting characteristic of the $Ca_V2.1$ C-terminal primary structure. SCA6 is caused by expansion of the polyQ tract in the human $Ca_V2.1$ gene from a normal repeat size range of 4–17 to a size range of 20–33 (34, 54, 66). To confirm the effect of polyQ expansion on the interaction between the $Ca_V2.1$ C terminus and RIM2α, association between YFP-tagged RIM2α and FLAG-tagged CTD of $Ca_V2.1$ (+44,47) Gln-40 with an elongated polyQ stretch of 40 residues was tested by co-IP in HEK293T cells (Fig. 9*A*). The intensity of the co-IP band for RIM2α normalized to the IP band for the CTD was moderately but significantly decreased for $Ca_V2.1$ CTD (+44,47) Gln-40 compared with that for $Ca_V2.1$ CTD (+44,47) with a polyQ stretch of 11 residues (Fig. 9*B*). To examine the effect of polyQ elongation on suppression of VDI by RIM2α, a recombinant P/Q-type VDCC was expressed as a complex of $Ca_V2.1$ (+44,47) with polyQ expansion ($Ca_V2.1$ (+44,47) Gln-40), β_4, and $\alpha_2\delta$-1 subunits in HEK293 cells (Fig. 9*C*). Without co-expression of α-RIMs, inactivation curves of whole-cell Ba^{2+} currents elicited by $Ca_V2.1$ (+44,47) and $Ca_V2.1$ (+44,47) Gln-40 were indistinguishable (Fig. 9*C* and Table 2). This contradicts with our previous report that polyQ expansion itself causes a hyperpolarizing shift of the inactivation curve for rabbit $Ca_V2.1$ channels carrying the β_1 subunit (67). It is possible that the effect of polyQ expansion on VDI depends on species and β subtypes (68). When RIM2α was co-expressed, inactivation curves of $Ca_V2.1$ (+44,47) and $Ca_V2.1$ (+44,47) Gln-40 were indistinguishable ($V_{0.5}$ of $Ca_V2.1$ (+44,47) Gln-40 and $Ca_V2.1$ (+44,47) were −11.0 ± 2.2 mV and −6.7 ± 2.3 mV, respectively) (Fig. 9*C* and Table 2). These data indicate that polyQ expansion reduced the binding affinity of $Ca_V2.1$ C terminus for RIM2α but not the suppressive effect of RIM2α on the VDI of $Ca_V2.1$ (+44,47).

Functional impacts of α-RIMs on VDI of N-type $Ca_V2.2$ and R-type $Ca_V2.3$ channels

Ca_V2 VDCCs are a major source of presynaptic Ca^{2+} influx (69–71), and α-RIMs also interact with the C terminus of $Ca_V2.2$ (22, 57). To explore the generality of our findings using $Ca_V2.1$, associations of the C-terminal region of $Ca_V2.2$

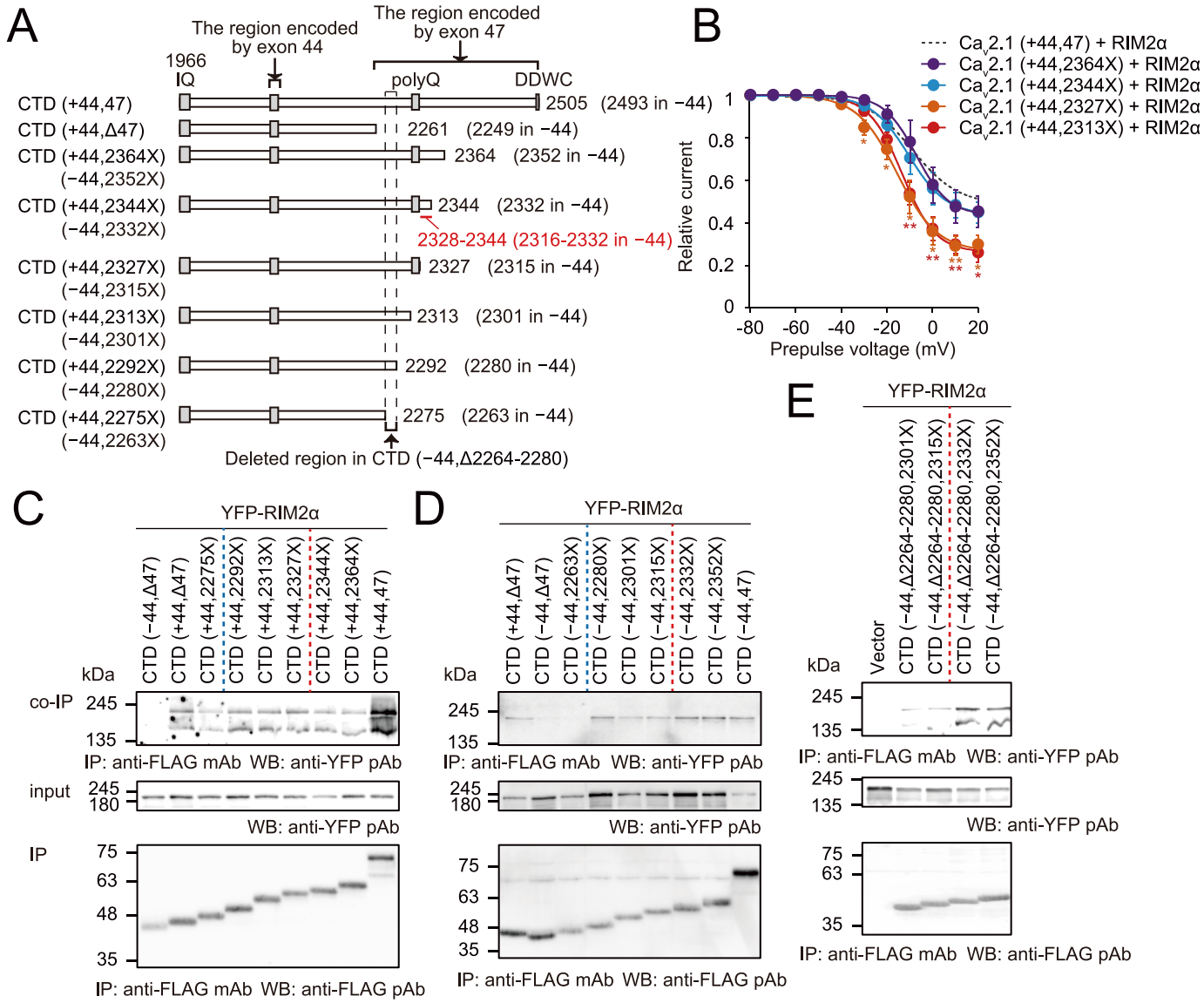

Figure 7. Identification of RIM2α-binding regions in the $Ca_V2.1$ C terminus. *A*, domain structures of $Ca_V2.1$ CTD deletion mutants. *B*, effects of RIM2α on inactivation curves of Ba^{2+} currents mediated by the deletion mutants of $Ca_V2.1$ (+44,47) in HEK293 cells expressing β_4 and $\alpha_2\delta$-1 subunits. The inactivation curve in cells co-expressing RIM2α and $Ca_V2.1$ (+44,47) (*dashed dark gray line*) is taken from Fig. 3 and is shown for comparison. *, $p < 0.05$; **, $p < 0.01$; statistical significance of differences *versus* cells co-expressing RIM2α and $Ca_V2.1$ (+44,47). See Table 5 for statistical significance of the differences. *Error bars,* S.E. *C*, interactions of FLAG-tagged $Ca_V2.1$ CTD (+44) deletion mutants with YFP-tagged RIM2α in HEK293T cells. *D*, interactions of FLAG-tagged $Ca_V2.1$ CTD (−44) deletion mutants with YFP-tagged RIM2α in HEK293T cells. *E*, interactions of FLAG-tagged $Ca_V2.1$ CTD (−44,Δ2264–2280) deletion mutants with YFP-tagged RIM2α in HEK293T cells. The interactions are evaluated by co-IP with monoclonal anti-FLAG antibody, followed by WB with polyclonal anti-YFP antibody. Input is 10% of the amount of cell lysate used for co-IP and is analyzed by WB using polyclonal anti-YFP antibody. IP of FLAG-tagged $Ca_V2.1$ CTDs with monoclonal anti-FLAG antibody is analyzed by WB using polyclonal anti-FLAG antibody. *Dashed lines* divide mutants in terms of co-IP level (*blue*) and inactivation curve (*red*).

encoded by exons 41–47 of the $Ca_V2.2$ gene ($Ca_V2.2$ CTD) and the C-terminal region of $Ca_V2.3$ encoded by exons 41–48 of the $Ca_V2.3$ gene ($Ca_V2.3$ CTD) with α-RIMs were tested by co-IP experiments. Both the YFP-tagged CTD of $Ca_V2.2$ and the YFP-tagged CTD of $Ca_V2.3$ were co-immunoprecipitated with FLAG-tagged α-RIMs in HEK293T cells (Fig. 10*A*). Thus, the C-terminal interaction with α-RIMs is shared by $Ca_V2.2$ and $Ca_V2.3$.

We also examined the effect of α-RIMs on the VDI of N-type VDCCs containing the $Ca_V2.2$, β_4, and $\alpha_2\delta$-1 subunits and of R-type VDCCs containing the $Ca_V2.3$, β_4, and $\alpha_2\delta$-1 subunits. In $Ca_V2.2$-expressing cells, α-RIMs significantly shifted $V_{0.5}$ values of the component susceptible to inactivation at high voltages ($V_{0.5}{}^{high}$) in inactivation curves of Ba^{2+} currents toward depolarizing potentials ($V_{0.5}{}^{high}$ of $Ca_V2.2$ co-transfected with vector, RIM1α, and RIM2α were −46.2 ± 3.0, −8.2 ± 14.8, and −2.8 ± 5.7 mV, respectively) (Fig. 10*B* and Table 6), as reported previously (20). RIM2α induced significant reduction of low voltage-inactivated phases (the ratios of low voltage-inactivating phases of $Ca_V2.2$ co-transfected with vector, RIM1α, and RIM2α were 0.64 ± 0.11, 0.63 ± 0.12, and 0.29 ± 0.05, respectively) (Fig. 10*B* and Table 6). Suppressive effects of α-RIMs on VDI were also observed for $Ca_V2.3$ (the ratios of inactivating components of $Ca_V2.3$ with co-transfection of vector, RIM1α, and RIM2α were 0.90 ± 0.03, 0.63 ± 0.09, and 0.67 ± 0.08, respectively). We failed to detect signifi-

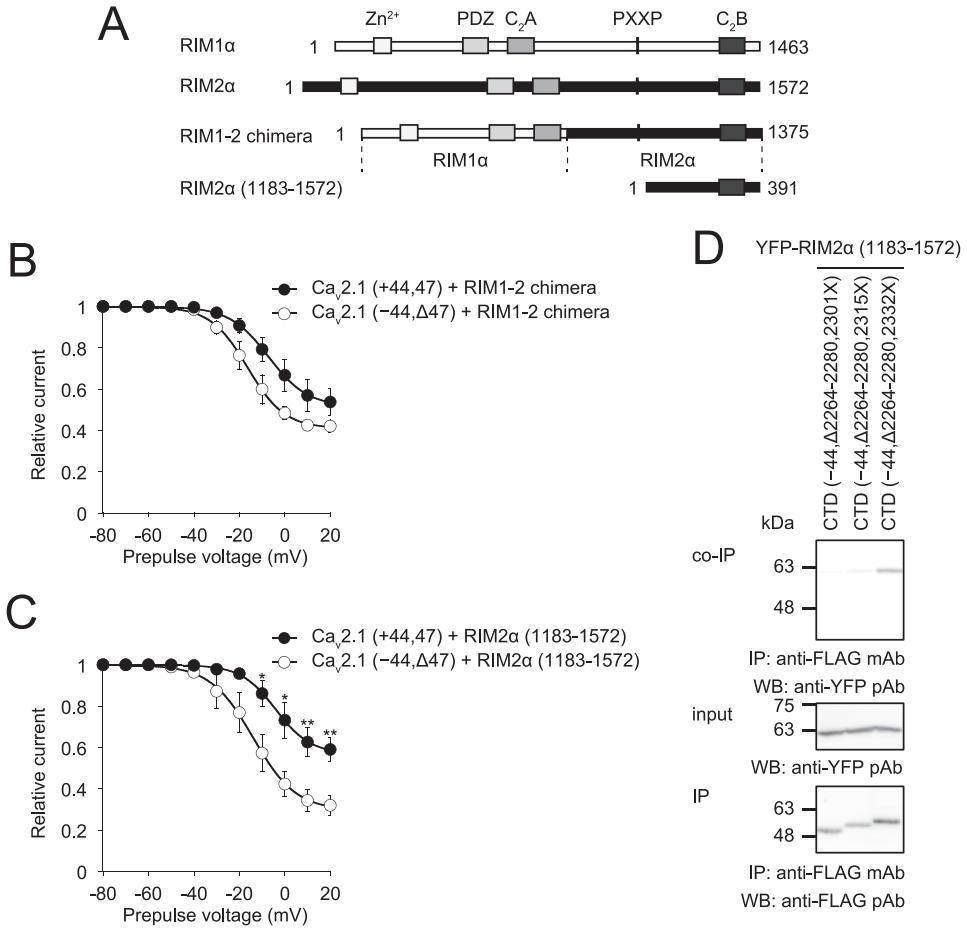

Figure 8. Identification of $Ca_V2.1$ C-terminal-binding region in RIM2α. *A,* domain structures of α-RIMs, RIM1–2 chimera, and RIM2α(1183–1572). *B* and *C,* effects of RIM1–2 chimera and RIM2α(1183–1572) on inactivation curves of Ba^{2+} currents mediated by $Ca_V2.1$ splice variants in HEK293 cells expressing β_4 and $\alpha_2\delta$-1 subunits. *, $p < 0.05$; **, $p < 0.01$; statistical significance of differences between $Ca_V2.1$ (−44,Δ47)-expressing and $Ca_V2.1$ (+44,47)-expressing cells. See Table 5 for statistical significance of the differences. *Error bars,* S.E. *D,* interactions of the deletion mutants of FLAG-tagged $Ca_V2.1$ (−44,Δ2264–2280) with YFP-tagged RIM2α(1183–1572) in HEK293T cells. The interactions are evaluated by co-IP with monoclonal anti-FLAG antibody, followed by WB with polyclonal anti-YFP antibody. Input is 10% of the amount of cell lysate used for co-IP and is analyzed by WB using polyclonal anti-YFP antibody. IP of FLAG-tagged $Ca_V2.1$ CTDs with monoclonal anti-FLAG antibody is analyzed by WB using polyclonal anti-FLAG antibody.

cant differences between the effect of RIM1α and RIM2α on VDI of $Ca_V2.3$ channels (Fig. 10*B* and Table 6). Thus, N-type $Ca_V2.2$ channels but not R-type $Ca_V2.3$ channels are susceptible to RIM2α-mediated potentiation of VDI suppression.

Discussion

In presynaptic AZs, where SVs dock in close vicinity to VDCCs at the presynaptic membrane, depolarization-induced Ca^{2+} influx via VDCCs triggers neurotransmitter release (1, 2). Previous proteomic analysis has shown that P/Q-, N-, and R-type VDCCs are embedded into protein networks assembled from a pool of 200 proteins (72). Unveiling the manner of protein-protein interactions in protein networks and their functional consequences is important for understanding the process of synapse formation and the modulation of synaptic transmission (73). Previously, we reported that α-RIMs increase neurotransmitter release by sustaining Ca^{2+} influx through strong inhibition of VDI of VDCCs and by anchoring vesicles in the vicinity of VDCCs via the RIM-β subunit interaction (20, 39). It has also been reported that α-RIMs interact with the $Ca_V2.1$ C-terminal region and modulate VDCCs targeting to presynaptic AZs (22). These previous studies have shown that RIM-VDCC interactions are key to the protein assembly responsible for stimulus-secretion coupling in presynaptic AZs.

Multipoint interaction plays important roles in the regulation of properties such as stabilization of protein complexes. In RIM-VDCC complexes, the significance of multipoint interaction has not yet been resolved. To approach this question, the contributions of each interaction should be quantitatively assessed. Our data strongly indicate that RIM-β subunit interaction is sufficient and necessary for α-RIMs to exert prominent suppressive effects of VDI of VDCCs, because in the $Ca_V2.1$ splice variant with the deletion of exons 44 and 47 ($Ca_V2.1$ (−44,Δ47)), strong VDI suppression remains intact for RIM1α, but for RIM2α it is attenuated to a level comparable with that of RIM1α. In the presynapse, VDCCs display a weak VDI (13, 30). Moreover, in the calyx of Held nerve terminals of RIM1 and RIM2 conditional double knock-out mice, depolarization pre-pulses induced stronger inactivation of VDCCs compared with wild-type mice (48).

$Ca_V2.1$ is known to be inactivated through at least two voltage-dependent mechanisms (fast and slow inactivation) (74). The mechanism underlying inactivation is not completely understood but may involve "hinged lid" or pore block-type

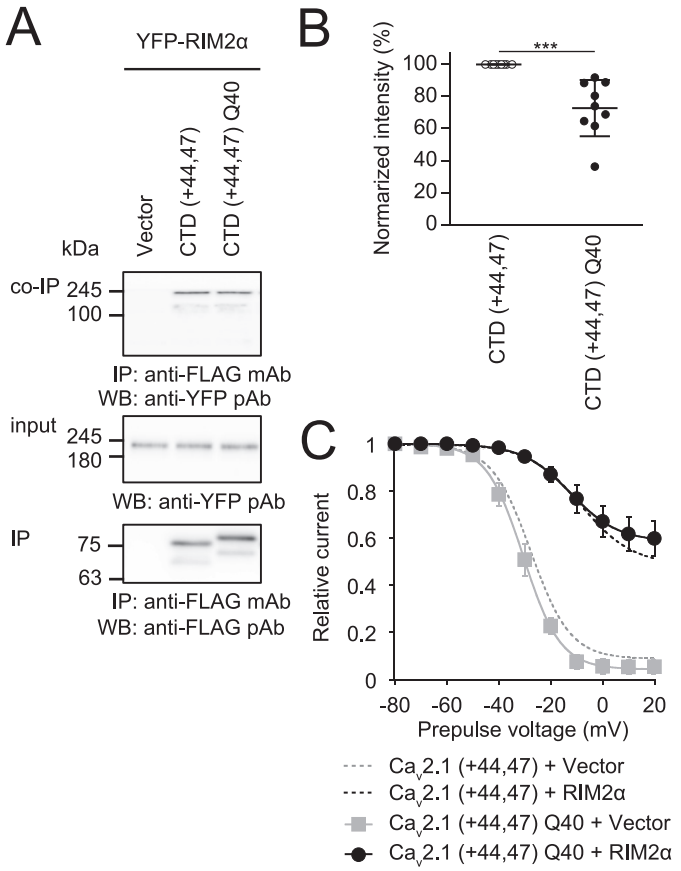

Figure 9. Effects of RIM2α on VDI of polyQ-elongated P/Q-type $Ca_V2.1$ channels. *A,* interaction of FLAG-tagged $Ca_V2.1$ CTD (+44,47) or (+44,47) Gln-40 (*Q40*) with YFP-tagged RIM2α in HEK293T cells. The interactions are evaluated by co-IP with monoclonal anti-FLAG antibody, followed by WB with polyclonal anti-YFP antibody. Input is 10% of the amount of cell lysate used for co-IP and is analyzed by WB using polyclonal anti-YFP antibody. IP of FLAG-tagged $Ca_V2.1$ CTDs with monoclonal anti-FLAG antibody is analyzed by WB using polyclonal anti-FLAG antibody. *B,* quantification of the data shown in *A*. The intensity of the co-IP band for RIM2α normalized to the IP band for the CTD ($Ca_V2.1$ CTD (+44,47), 100%; $Ca_V2.1$ CTD (+44,47) Gln-40, 73 ± 18%) (92). Data for nine experiments are presented in scatter plots. The *vertical error bars* represent standard deviations, and the mean values are indicated with *horizontal bars*. ***, $p < 0.001$; statistical significance of difference between CTD (+44,47) and CTD (+44,47) Gln-40. *C,* effects of RIM2α on inactivation curves of P/Q-type $Ca_V2.1$ (+44,47) Gln-40 currents in HEK293 cells expressing β_4 and $\alpha_2\delta$-1 subunits. The inactivation curves in cells co-expressing vector and $Ca_V2.1$ (+44,47) (*dashed gray line*) and in cells co-expressing RIM2α and $Ca_V2.1$ (+44,47) (*dashed dark gray line*) are taken from Fig. 3 and are shown for comparison. See Table 2 for statistical significance of the differences. *Error bars,* S.E.

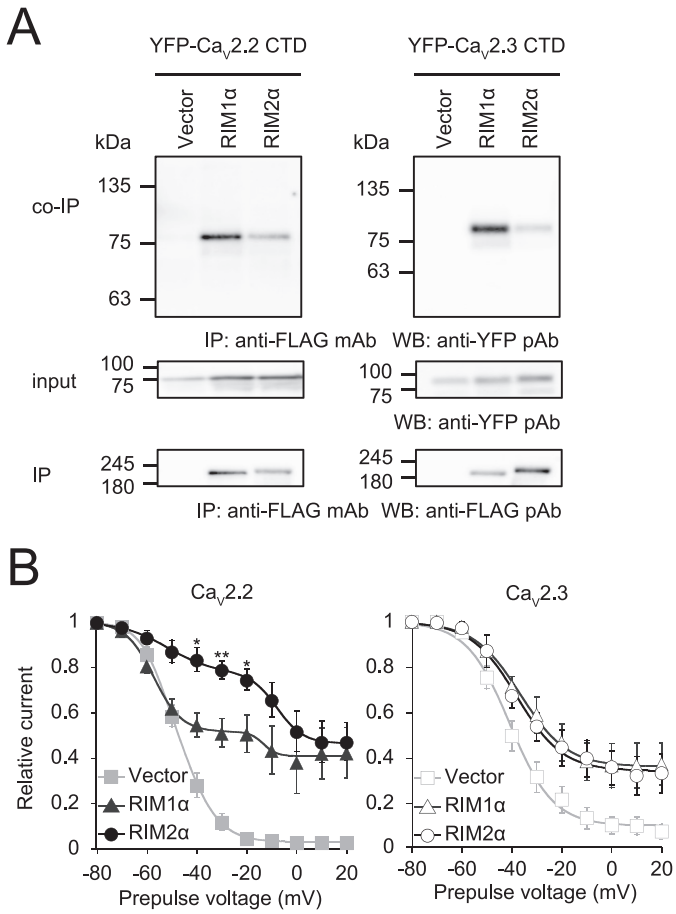

Figure 10. Effects of α-RIMs on VDI of N-type $Ca_V2.2$ and R-type $Ca_V2.3$ channels. *A,* interactions of YFP-tagged $Ca_V2.2$ CTD or $Ca_V2.3$ CTD with FLAG-tagged α-RIMs in HEK293T cells. The interactions are evaluated by co-IP with monoclonal anti-FLAG antibody, followed by WB with polyclonal anti-YFP antibody. Input is 10% of the amount of cell lysate used for co-IP and is analyzed by WB using polyclonal anti-YFP antibody. IP of FLAG-tagged α-RIMs with monoclonal anti-FLAG antibody is analyzed by WB using polyclonal anti-FLAG antibody. *B,* effects of α-RIMs on inactivation curves of N-type $Ca_V2.2$ and R-type $Ca_V2.3$ currents in HEK293 cells expressing β_4 and $\alpha_2\delta$-1 subunits. See Table 6 for statistical significance of the differences. *, $p < 0.05$; **, $p < 0.01$; statistical significance of differences between RIM1α- and RIM2α-expressing cells. *Error bars,* S.E.

mechanisms (75–77). It has also been reported that fast and slow inactivation represents structurally independent conformational changes (78). Our kinetic analyses of current decay showed that both RIM1α and RIM2α decreased the fast inactivation component and increased τ_{slow} regardless of the presence of the exon 44 and 47 regions in $Ca_V2.1$ (Fig. 5, *C* and *D*), although only RIM2α (but not RIM1α) increased τ_{fast} in the presence of the exon 44 and 47 regions in $Ca_V2.1$ (Fig. 5*C*). These findings may suggest that the interaction between $Ca_V2.1$ CTD and RIM2α induces conformational changes of the VDCC $Ca_V2.1$ α_1 subunit in addition to those induced by the interaction between β subunit and α-RIMs.

By focusing on the splice variants of the $Ca_V2.1$ C-terminal region, we have deepened our understanding of the interaction between VDCCs and α-RIMs. α-RIMs interact with the $Ca_V2.1$ C-terminal region via the regions encoded by exons 44 and 47, the alternative splicing of which generates major C-terminal variants in the human cerebellum. Our experiments revealed at least four regions in the $Ca_V2.1$ CTD involved in interaction with RIM2α: a site encoded by exon 44 and three sites in the region encoded by exon 47. Analysis of relative mRNA levels of these $Ca_V2.1$ C-terminal splice variants indicates that 56, 86, or 67% of the total $Ca_V2.1$ mRNA carries either both exons 44 and 47, exon 44 alone, or exon 47 alone, respectively (Table 1). These spliced mRNAs are capable of encoding the $Ca_V2.1$ variants that interact with α-RIMs. The effect of RIM2α-$Ca_V2.1$ C-terminal interaction on VDI can be generated from 67% of the total $Ca_V2.1$ mRNA. Interestingly, there is a wide range of fundamental properties for individual synapses, including release probability, unitary response, and effects of previous stimulation on subsequent response (79). This suggests that $Ca_V2.1$ C-terminal splice variants may contribute to the heterogeneous molecular composition and function of VDCCs in

Table 6
Effect of α-RIMs on inactivation properties of N-type and R-type VDCCs in HEK293 cells expressing $Ca_V2.2$ or $Ca_V2.3$, α_2/δ-1, and β_4
*, $p < 0.05$; ***, $p < 0.001$ *versus* vector. #, $p < 0.05$ *versus* RIM1. The number of cells analyzed are indicated in parentheses.

		Inactivation parameters					
		a	$V_{0.5}^{low}$	K^{low}	*b*	$V_{0.5}^{high}$	K^{high}
			mV	*mV*		*mV*	*mV*
$Ca_V2.2$	Vector	0.64 ± 0.11 (4)	−50.2 ± 1.6 (4)	−7.4 ± 0.8 (4)	0.32 ± 0.11 (4)	−46.2 ± 3.0 (4)	−3.9 ± 1.7 (4)
	RIM1α	0.63 ± 0.12 (4)	−52.7 ± 5.7 (4)	−8.4 ± 2.1 (4)	0.06 ± 0.14 (4)	−8.2 ± 14.8 (4)*	−10.6 ± 6.3 (4)
	RIM2α	0.29 ± 0.05 (5)*, #	−46.5 ± 7.6 (5)	−11.1 ± 4.4 (5)	0.21 ± 0.07 (5)	−2.8 ± 5.7 (5)***	−2.0 ± 1.6 (5)
$Ca_V2.3$	Vector	0.90 ± 0.03 (4)	−40.5 ± 2.6 (4)	−8.5 ± 0.6 (4)			
	RIM1α	0.63 ± 0.09 (4)*	−36.0 ± 2.5 (4)	−9.1 ± 1.2 (4)			
	RIM2α	0.67 ± 0.08 (4)*	−37.3 ± 3.8 (4)	−9.3 ± 1.7 (4)			

presynaptic AZs. Importantly, a recent study has suggested that tissue-regulated alternatively spliced exons are significantly enriched in flexible regions of proteins that form conserved interaction surfaces to establish tissue-dependent protein-protein interaction networks (80). It is therefore possible that arrangements of presynaptic proteins that include VDCC subunits may be precisely coordinated via protein-protein interactions through the regions encoded by alternatively spliced exons 44 and 47. In terms of the effect of α-RIMs on VDCC channel properties, the interaction between RIM2α and the 17 amino acid residues, 2328–2344, of $Ca_V2.1$ (+44,47) in the region encoded by exon 47 of $Ca_V2.1$ is responsible for potentiation of VDI suppression (Fig. 7, *B* and *E*). In contrast, the interaction between α-RIMs and the region encoded by exon 44 of $Ca_V2.1$ failed to exert any significant effect on VDCC channel properties (Fig. 3*B*). Alternative splicing of exons 44 and 47 may contribute to the fine adjustment of RIM-VDCC complexes that can affect neurotransmitter release from AZs of different types of presynapses.

The interaction between the $Ca_V2.1$ C terminus and RIM-BPs, which bind to α-RIMs, is important for the coupling of SVs, VDCCs, and the SV fusion machinery (19, 81). The AZ protein Bassoon interacts with both β subunits and RIM-BPs to regulate $Ca_V2.1$ targeting to the AZ (9, 82–84). The β subunits are also known to directly interact with the $Ca_V2.1$ C terminus (85). These findings may inform the physiological significance of interactions among the $Ca_V2.1$ C-terminal region, β subunits, and α-RIMs. Interestingly, the RIM-BP-binding region in the $Ca_V2.1$ C-terminal region is the proline-rich region (P*XX*P) in amino acid residues 2276–2292 of $Ca_V2.1$ (+44,47), which is a RIM2α-binding region in the region encoded by exon 47 (19). Previous studies have revealed that the amino acid residues 2502–2505 of $Ca_V2.1$ (+44,47) bind to α-RIMs (22) and are essential for interaction with Mint1 (56). These results raise the possibility that the $Ca_V2.1$ C-terminal region is the target of AZ scaffolding proteins and that their competitive binding underlies dynamic properties of AZ protein networks in the molecular processes of neurotransmitter release.

Notably, both RIM1α and RIM2α bind to the C-terminal regions of $Ca_V2.1$, $Ca_V2.2$, and $Ca_V2.3$ (Figs. 2*D* and 10*A*), but potentiation of the suppressive effect on VDI was only observed for $Ca_V2.1$ or $Ca_V2.2$ combined with RIM2α (Figs. 3*B* and 10*B*). As already mentioned above, among four regions in the $Ca_V2.1$ CTD involved in interaction with RIM2α, the two regions of $Ca_V2.1$ CTD (the amino acid residues 2276–2292 and 2502–2505 of $Ca_V2.1$ (+44,47)) are highly conserved among the three Ca_V2 isoforms (supplemental Fig. 1). It has been shown that Bassoon localizes $Ca_V2.1$ but not $Ca_V2.2$ to AZs via molecular interaction with RIM-BPs (9), despite the fact that RIM-BPs can also interact with the P*XX*P motif of $Ca_V2.2$ (19). Furthermore, mutation of the PDZ-binding motif of EGFP-tagged $Ca_V2.1$ failed to affect the localization pattern of $Ca_V2.1$ in cultured mouse hippocampal neurons (86). These results indicate that the functions of some protein-protein interactions are dependent on other components and that use of appropriate assay systems and neuronal types is necessary to reveal their functionality.

From a pathological point of view, it is interesting that mutations associated with genetic diseases in the genes encoding RIMs modify their function in regulating VDCC currents (50, 51). In SCA6 patients, the relative mRNA level of the $Ca_V2.1$ splice variant, which possesses exon 47, is increased in cerebellar Purkinje cells but not in granule cells (87). In several episodic ataxia type 2 patients, mutations in $Ca_V2.1$ result in the loss of the regions encoded by exons 44 and 47 (32). These two diseases have similar symptoms, such as ataxic gait and loss of limb coordination. Although our results showed that the polyQ elongation itself does not affect functional regulation of VDCCs by RIM2α, increase in the relative proportion of the $Ca_V2.1$ splice variants that possess the region encoded by exon 47 may cause excessive RIM2α functional regulation. Dysregulation of the molecular organization of presynaptic AZs containing VDCC complexes may lead to abnormalities in different functional hierarchies of nervous system.

Experimental procedures

cDNA cloning and construction of expression vectors

Mouse RIM1α, mouse RIM2α, mouse $Ca_V2.2$, rabbit $\alpha_2\delta$, human $Ca_V2.1$ (−44,Δ47), and rat $Ca_V2.3$ have been described previously (20, 39, 50, 88, 89). Human VDCC β_4 subunit (GenBank™ accession number NM_001005747) was cloned using PCR from human whole-brain Marathon-Ready cDNA (Clontech) and was subcloned into pcDNA™3.1 (−) vector (Thermo Fisher Scientific). For production of YFP fusion proteins for RIM1α, RIM2α, CTD (amino acid residues 1855–2327) of $Ca_V2.2$ (GenBank™ accession number NM_001042528), and CTD (amino acid residues 1860–2295) of $Ca_V2.3$ (GenBank™ accession number NM_019294), cDNAs for these constructs and the YFP were subcloned together into the pCI-neo vector (Promega). For production of YFP fusion protein for β_4, cDNAs for β_4 construct and the YFP were subcloned together into the pcDNA™3.1(−) vector. CTD (amino acid residues 1966–2505) of human $Ca_V2.1$ (+44,47)

(GenBank™ accession number U79666) was cloned using PCR from human whole-brain Marathon-Ready cDNA (Clontech) and was subcloned into the FLAG-tagged vector pCMV-tag2 (Stratagene) and human $Ca_V2.1$ (−44,Δ47) clone. To construct CTD of $Ca_V2.1$ (+44,47) Gln-40, the ApaI(7152)–MscI(7196) fragment containing 11 CAG repeats was replaced with synthetic oligonucleotides containing 40 CAG repeats. CTD of human $Ca_V2.1$ splice variants with different combinations of exons 44 and 47 were constructed by PCR and were subcloned into pCMV-tag2 and human $Ca_V2.1$ (+44,47) clone. Mutants or chimeras of CTD of $Ca_V2.1$ and α-RIMs were constructed by PCR.

Cell culture and cDNA expression in HEK293 or HEK293T cells

HEK293 and HEK293T cells were cultured in Dulbecco's modified Eagle's medium containing 10% fetal bovine serum, 30 units/ml penicillin, and 30 μg/ml streptomycin at 37 °C under 5% CO_2. Transfection of cDNA plasmids was carried out using SuperFect Transfection Reagent (Qiagen). For electrophysiological measurements, recombinant plasmids were co-transfected with pIRES2-EGFP (Clontech), and HEK293 cells with green fluorescence were analyzed. Transfected cells were grown for 36–48 h before electrophysiological measurements and co-IP assay.

Characterization of splice variation of $Ca_V2.1$ C terminus in the human cerebellum by sequence analysis

We designed PCR oligonucleotide primers as follows: forward in the exon 42, 5′-GCTGGTCACACCTCACAAG-3′, and reverse in the exon 47, 5′-GCTGGGCTTCCACTTACG-3′. Temperature cycles were as follows. Temperature initially 98 °C for 2 min was followed by 25 cycles at 98 °C for 10 s, 64 °C for 30 s, and 68 °C for 1 min. The PCR products from human cerebellum cDNA (Takara, 9523) were electrophoresed on an 1% agarose gel, cut out, purified using the QiaexII gel extraction kit (Qiagen), and ligated into the EcoRV-digested pBluescript II SK(−) (Stratagene). The ligation products were transformed into competent *Escherichia coli* DH5α cells and screened on Luria-Bertani plates containing ampicillin, X-Gal, and isopropyl β-D-1-thiogalactopyranoside for 15–20 h at 37 °C. White colonies were picked randomly and subjected to sequencing analyses using T7 and M13-reverse universal sequencing primers. The sequencing results were analyzed by using BioEdit software version 7.2.5.

Yeast two-hybrid screening and β-galactosidase assay

We subcloned CTD of human $Ca_V2.1$ (+44,47) into pGBK-T7 and used it as a bait to screen a human brain pACT2 library (Clontech) in the yeast strain AH109 (Clontech). We plated transformants (2.5×10^6) on synthetic medium lacking adenine, histidine, leucine, and tryptophan and assayed His^+ colonies for β-galactosidase activity with a filter assay. Of the transformants, 56 were His^+, and 6 of these were also $LacZ^+$. We isolated prey clone encoding amino acid residues 487–1349 of RIM2α (GenBank™ accession number NM_001100117).

co-IP assay in HEK293T cells

36–48 h after transfection, HEK293T cells were solubilized in Nonidet P-40 buffer (150 mM NaCl, 50 mM Tris, 1% Nonidet P-40, and 1 mM PMSF) and then centrifuged at 17,400 × *g* for 20 min. The cell lysate was incubated with anti-FLAG M2 monoclonal antibody (Sigma, F3165), and then the immunocomplexes were incubated with protein A-agarose beads (Santa Cruz Biotechnology, SC-2001), and the beads were washed with Nonidet P-40 buffer. The co-immunoprecipitated and immunoprecipitated proteins were characterized by Western blotting (WB) with anti-YFP antibody (Clontech, 632592) and anti-FLAG antibody (Sigma, F7425), respectively. Input was 10% of the amount of cell lysate used for co-IP and was characterized by WB with anti-YFP antibody. The chemiluminescence intensities of the bands were measured by Multigauge version 3.0 (Fuji film).

Current recordings

Whole-cell mode of the patch-clamp technique was carried out at 22–25 °C with an EPC-10 (HEKA Elektronik) patch-clamp amplifier as described previously (39, 41, 90). Patch pipettes were made from borosilicate glass capillaries (1.5-mm outer diameter, 0.87-mm inner diameter; Hilgenberg) using a model P-97 Flaming-Brown micropipette puller (Sutter Instrument Co.). The patch electrodes were fire-polished. Pipette resistance ranged from 2 to 4 megohms when filled with the pipette solutions described below. The series resistance was electronically compensated to >60%, and both the leakage and the remaining capacitance were subtracted by the −P/4 method. Currents were sampled at 10 kHz after low-pass filtering at 3.0 kHz (3 db) in the experiments of inactivation kinetics and AP-like trains, otherwise sampled at 20 kHz after low-pass filtering at 3.0 kHz (3 db). Data were collected and analyzed using Patchmaster (HEKA Elektronik) software. An external solution contained 5 mM $BaCl_2$, 148 mM tetraethylammonium chloride, 10 mM HEPES, and 10 mM glucose (pH 7.4-adjusted with tetraethylammonium-OH). The pipette solution contained 95 mM CsOH, 95 mM aspartate, 40 mM CsCl, 4 mM $MgCl_2$, 5 mM EGTA, 2 mM disodium ATP, 5 mM HEPES, and 8 mM creatine phosphate (pH 7.2-adjusted with CsOH).

Voltage dependence of inactivation

To determine the inactivation curve of VDCCs, Ba^{2+} currents were evoked by 40-ms test pulse to 10 mV after the 10-ms repolarization to −90 mV following 1-s (300 ms for $Ca_V2.3$) prepulse voltage (V_{pre}) displacement (conditioning pulse) from −80 to 20 mV with 10-mV increments. Amplitudes of currents elicited by the test pulses were normalized to those elicited by the test pulse after a 1-s V_{pre} displacement to −80 mV. The mean values were plotted against potentials of the 1-s V_{pre} displacement. When the inactivation curve was monophasic, the mean values were fitted to the single Boltzmann equation, $h(V_{pre}) = (1 - a) + a/(1 + \exp((V_{0.5} - V_{pre})/k))$, where a is the rate of inactivating component; $V_{0.5}$ is the potential to give a half-value of inactivation; and k is the slope factor. Otherwise, the mean values were fitted to the sum of two Boltzmann equations: $h(V_{pre}) = (1 - a - b) + a/(1 + \exp((V_{0.5}{}^{low} - V_{pre})/k^{low})) + b/(1 + \exp((V_{0.5}{}^{high} - V_{pre})/k^{high}))$, where a, b, and $(1 - a - b)$ are the ratios of a low voltage-induced phase, a high voltage-induced phase, and a non-inactivating phase; $V_{0.5}{}^{low}$ and $V_{0.5}{}^{high}$ are the potentials that give a half-value of components

susceptible to inactivation at low voltages in inactivation curves and at high voltages; and k^{low} and k^{high} are the slope factors. The decay phase of Ba^{2+} currents evoked by 1-s test pulses was fitted by two (fast and slow) exponential functions with a non-inactivating component: $-I(t) = a + b\exp(-\lambda_1 t) + c\exp(-\lambda_2 t)$, where $I(t)$ is the inactivating current as a function of time; a is the current amplitude at $t = \infty$; b and c are the amplitudes of the time-dependent components; and λ_1 and λ_2 are the reciprocals of the fast (τ_{fast}) and the slow (τ_{slow}) time constants of inactivation, respectively (41, 91). APs began at −80 mV and peaked at 33 mV. Rising and falling slopes were 283 and −103 V/s, respectively (20, 65). Leaks and capacitive transients were subtracted by a −P/4 protocol.

I-V relationships

The individual activation data were fitted to standard Boltzmann equation in the form $I_{Ba} = G_{max}(V_m - V_{rev})/(1 + \exp(-(V_m - V_{0.5})/k))$, where G_{max} is the maximal conductance; V_m is the membrane voltage; V_{rev} is the I_{Ba} reversal potential; $V_{0.5}$ is the half-activation potential, and k is the slope factor.

Statistical analysis

All data are expressed as the means ± S.E. The statistical analyses were performed using Student's t test. A value of $p < 0.05$ was considered significant.

Author contributions—M. H. designed the study, conducted most of the experiments, analyzed the results, and wrote most of the paper. Y. T. collected preliminary data and constructed vectors. K. Y. and C. F. W. conducted and analyzed the experiments on co-IP. H. K. conducted the sequence analysis of PCR products from the human cerebellum cDNA library. T. K., M. X. M., T. P. S., M. R., M. D. W., and Y. M. directed the research, wrote the manuscript, analyzed, interpreted the data, and critically reviewed the manuscript.

Acknowledgments—We thank S. Kiyonaka, T. Numata, R. Sakaguchi, and N. Ogawa for experimental advice and helpful discussions.

References

1. Ackermann, F., Waites, C. L., and Garner, C. C. (2015) Presynaptic active zones in invertebrates and vertebrates. *EMBO Rep.* **16,** 923–938
2. Jahn, R., and Fasshauer, D. (2012) Molecular machines governing exocytosis of synaptic vesicles. *Nature* **490,** 201–207
3. Tsien, R. W., Lipscombe, D., Madison, D. V., Bley, K. R., and Fox, A. P. (1988) Multiple types of neuronal calcium channels and their selective modulation. *Trends Neurosci.* **11,** 431–438
4. Birnbaumer, L., Campbell, K. P., Catterall, W. A., Harpold, M. M., Hofmann, F., Horne, W. A., Mori, Y., Schwartz, A., Snutch, T. P., and Tanabe, T. (1994) The naming of voltage-gated calcium channels. *Neuron* **13,** 505–506
5. Takahashi, T., and Momiyama, A. (1993) Different types of calcium channels mediate central synaptic transmission. *Nature* **366,** 156–158
6. Wu, L. G., Borst, J. G., and Sakmann, B. (1998) R-type Ca^{2+} currents evoke transmitter release at a rat central synapse. *Proc. Natl. Acad. Sci. U.S.A.* **95,** 4720–4725
7. Fox, A. P., Nowycky, M. C., and Tsien, R. W. (1987) Single-channel recordings of three types of calcium channels in chick sensory neurones. *J. Physiol.* **394,** 173–200
8. Weber, A. M., Wong, F. K., Tufford, A. R., Schlichter, L. C., Matveev, V., and Stanley, E. F. (2010) N-type Ca^{2+} channels carry the largest current: implications for nanodomains and transmitter release. *Nat. Neurosci.* **13,** 1348–1350
9. Davydova, D., Marini, C., King, C., Klueva, J., Bischof, F., Romorini, S., Montenegro-Venegas, C., Heine, M., Schneider, R., Schröder, M. S., Altrock, W. D., Henneberger, C., Rusakov, D. A., Gundelfinger, E. D., and Fejtova, A. (2014) Bassoon specifically controls presynaptic P/Q-type Ca^{2+} channels via RIM-binding protein. *Neuron* **82,** 181–194
10. Parajuli, L. K., Nakajima, C., Kulik, A., Matsui, K., Schneider, T., Shigemoto, R., and Fukazawa, Y. (2012) Quantitative regional and ultrastructural localization of the $Ca_V2.3$ subunit of R-type calcium channel in mouse brain. *J. Neurosci.* **32,** 13555–13567
11. Holderith, N., Lorincz, A., Katona, G., Rózsa, B., Kulik, A., Watanabe, M., and Nusser, Z. (2012) Release probability of hippocampal glutamatergic terminals scales with the size of the active zone. *Nat. Neurosci.* **15,** 988–997
12. Kulik, A., Nakadate, K., Hagiwara, A., Fukazawa, Y., Luján, R., Saito, H., Suzuki, N., Futatsugi, A., Mikoshiba, K., Frotscher, M., and Shigemoto, R. (2004) Immunocytochemical localization of the a_{1A} subunit of the P/Q-type calcium channel in the rat cerebellum. *Eur. J. Neurosci.* **19,** 2169–2178
13. Forsythe, I. D., Tsujimoto, T., Barnes-Davies, M., Cuttle, M. F., and Takahashi, T. (1998) Inactivation of presynaptic calcium current contributes to synaptic depression at a fast central synapse. *Neuron* **20,** 797–807
14. Inchauspe, C. G., Martini, F. J., Forsythe, I. D., and Uchitel, O. D. (2004) Functional compensation of P/Q by N-type channels blocks short-term plasticity at the calyx of Held presynaptic terminal. *J. Neurosci.* **24,** 10379–10383
15. Ishikawa, T., Kaneko, M., Shin, H. S., and Takahashi, T. (2005) Presynaptic N-type and P/Q-type Ca^{2+} channels mediating synaptic transmission at the calyx of Held of mice. *J. Physiol.* **568,** 199–209
16. Miki, T., Hirai, H., and Takahashi, T. (2013) Activity-dependent neurotrophin signaling underlies developmental switch of Ca^{2+} channel subtypes mediating neurotransmitter release. *J. Neurosci.* **33,** 18755–18763
17. Ertel, E. A., Campbell, K. P., Harpold, M. M., Hofmann, F., Mori, Y., Perez-Reyes, E., Schwartz, A., Snutch, T. P., Tanabe, T., Birnbaumer, L., Tsien, R. W., and Catterall, W. A. (2000) Nomenclature of voltage-gated calcium channels. *Neuron* **25,** 533–535
18. Catterall, W. A., and Few, A. P. (2008) Calcium channel regulation and presynaptic plasticity. *Neuron* **59,** 882–901
19. Hibino, H., Pironkova, R., Onwumere, O., Vologodskaia, M., Hudspeth, A. J., and Lesage, F. (2002) RIM binding proteins (RBPs) couple Rab3-interacting molecules (RIMs) to voltage-gated Ca^{2+} channels. *Neuron* **34,** 411–423
20. Kiyonaka, S., Wakamori, M., Miki, T., Uriu, Y., Nonaka, M., Bito, H., Beedle, A. M., Mori, E., Hara, Y., De Waard, M., Kanagawa, M., Itakura, M., Takahashi, M., Campbell, K. P., and Mori, Y. (2007) RIM1 confers sustained activity and neurotransmitter vesicle anchoring to presynaptic Ca^{2+} channels. *Nat. Neurosci.* **10,** 691–701
21. Geppert, M., Goda, Y., Hammer, R. E., Li, C., Rosahl, T. W., Stevens, C. F., and Südhof, T. C. (1994) Synaptotagmin I: a major Ca^{2+} sensor for transmitter release at a central synapse. *Cell* **79,** 717–727
22. Kaeser, P. S., Deng, L., Wang, Y., Dulubova, I., Liu, X., Rizo, J., and Südhof, T. C. (2011) RIM proteins tether Ca^{2+} channels to presynaptic active zones via a direct PDZ-domain interaction. *Cell* **144,** 282–295
23. Sheng, Z. H., Rettig, J., Takahashi, M., and Catterall, W. A. (1994) Identification of a syntaxin-binding site on N-type calcium channels. *Neuron* **13,** 1303–1313
24. Bezprozvanny, I., Scheller, R. H., and Tsien, R. W. (1995) Functional impact of syntaxin on gating of N-type and Q-type calcium channels. *Nature* **378,** 623–626
25. Bachnoff, N., Cohen-Kutner, M., Trus, M., and Atlas, D. (2013) Intramembrane signaling between the voltage-gated Ca^{2+}-channel and cysteine residues of syntaxin 1A coordinates synchronous release. *Sci. Rep.* **3,** 1620
26. Kaeser, P. S., and Regehr, W. G. (2014) Molecular mechanisms for synchronous, asynchronous, and spontaneous neurotransmitter release. *Annu. Rev. Physiol.* **76,** 333–363

27. Wang, L. Y., and Augustine, G. J. (2014) Presynaptic nanodomains: a tale of two synapses. *Front. Cell. Neurosci.* **8,** 455
28. Sheng, J., He, L., Zheng, H., Xue, L., Luo, F., Shin, W., Sun, T., Kuner, T., Yue, D. T., and Wu, L. G. (2012) Calcium-channel number critically influences synaptic strength and plasticity at the active zone. *Nat. Neurosci.* **15,** 998–1006
29. Simms, B. A., and Zamponi, G. W. (2014) Neuronal voltage-gated calcium channels: structure, function, and dysfunction. *Neuron* **82,** 24–45
30. Stanley, E. F. (2003) Syntaxin I modulation of presynaptic calcium channel inactivation revealed by botulinum toxin C1. *Eur. J. Neurosci.* **17,** 1303–1305
31. Mori, Y., Friedrich, T., Kim, M. S., Mikami, A., Nakai, J., Ruth, P., Bosse, E., Hofmann, F., Flockerzi, V., Furuichi, T., Mikoshiba, K., Imoto, K., Tanabe, T., and Numa, S. (1991) Primary structure and functional expression from complementary DNA of a brain calcium channel. *Nature* **350,** 398–402
32. Pietrobon, D. (2010) $Ca_V2.1$ channelopathies. *Pflugers Arch.* **460,** 375–393
33. Ophoff, R. A., Terwindt, G. M., Vergouwe, M. N., van Eijk, R., Oefner, P. J., Hoffman, S. M., Lamerdin, J. E., Mohrenweiser, H. W., Bulman, D. E., Ferrari, M., Haan, J., Lindhout, D., van Ommen, G. J., Hofker, M. H., Ferrari, M. D., and Frants, R. R. (1996) Familial hemiplegic migraine and episodic ataxia type-2 are caused by mutations in the Ca^{2+} channel gene CACNL1A4. *Cell* **87,** 543–552
34. Zhuchenko, O., Bailey, J., Bonnen, P., Ashizawa, T., Stockton, D. W., Amos, C., Dobyns, W. B., Subramony, S. H., Zoghbi, H. Y., and Lee, C. C. (1997) Autosomal dominant cerebellar ataxia (SCA6) associated with small polyglutamine expansions in the α_{1A}-voltage-dependent calcium channel. *Nat. Genet.* **15,** 62–69
35. Bourinet, E., Soong, T. W., Sutton, K., Slaymaker, S., Mathews, E., Monteil, A., Zamponi, G. W., Nargeot, J., and Snutch, T. P. (1999) Splicing of α_{1A} subunit gene generates phenotypic variants of P- and Q-type calcium channels. *Nat. Neurosci.* **2,** 407–415
36. Stea, A., Tomlinson, W. J., Soong, T. W., Bourinet, E., Dubel, S. J., Vincent, S. R., and Snutch, T. P. (1994) Localization and functional properties of a rat brain α_{1A} calcium channel reflect similarities to neuronal Q- and P-type channels. *Proc. Natl. Acad. Sci. U.S.A.* **91,** 10576–10580
37. Yokoyama, C. T., Myers, S. J., Fu, J., Mockus, S. M., Scheuer, T., and Catterall, W. A. (2005) Mechanism of SNARE protein binding and regulation of Cav2 channels by phosphorylation of the synaptic protein interaction site. *Mol. Cell. Neurosci.* **28,** 1–17
38. Tsunemi, T., Saegusa, H., Ishikawa, K., Nagayama, S., Murakoshi, T., Mizusawa, H., and Tanabe, T. (2002) Novel $Ca_V2.1$ splice variants isolated from Purkinje cells do not generate P-type Ca^{2+} current. *J. Biol. Chem.* **277,** 7214–7221
39. Uriu, Y., Kiyonaka, S., Miki, T., Yagi, M., Akiyama, S., Mori, E., Nakao, A., Beedle, A. M., Campbell, K. P., Wakamori, M., and Mori, Y. (2010) Rab3-interacting molecule γ isoforms lacking the Rab3-binding domain induce long lasting currents but block neurotransmitter vesicle anchoring in voltage-dependent P/Q-type Ca^{2+} channels. *J. Biol. Chem.* **285,** 21750–21767
40. Randall, A., and Tsien, R. W. (1995) Pharmacological dissection of multiple types of Ca^{2+} channel currents in rat cerebellar granule neurons. *J. Neurosci.* **15,** 2995–3012
41. Wakamori, M., Yamazaki, K., Matsunodaira, H., Teramoto, T., Tanaka, I., Niidome, T., Sawada, K., Nishizawa, Y., Sekiguchi, N., Mori, E., Mori, Y., and Imoto, K. (1998) Single tottering mutations responsible for the neuropathic phenotype of the P-type calcium channel. *J. Biol. Chem.* **273,** 34857–34867
42. Kanumilli, S., Tringham, E. W., Payne, C. E., Dupere, J. R., Venkateswarlu, K., and Usowicz, M. M. (2006) Alternative splicing generates a smaller assortment of $Ca_V2.1$ transcripts in cerebellar Purkinje cells than in the cerebellum. *Physiol. Genomics* **24,** 86–96
43. Südhof, T. C. (2012) The presynaptic active zone. *Neuron* **75,** 11–25
44. Schoch, S., Castillo, P. E., Jo, T., Mukherjee, K., Geppert, M., Wang, Y., Schmitz, F., Malenka, R. C., and Südhof, T. C. (2002) RIM1α forms a protein scaffold for regulating neurotransmitter release at the active zone. *Nature* **415,** 321–326
45. Gracheva, E. O., Hadwiger, G., Nonet, M. L., and Richmond, J. E. (2008) Direct interactions between C. elegans RAB-3 and Rim provide a mechanism to target vesicles to the presynaptic density. *Neurosci. Lett.* **444,** 137–142
46. Koushika, S. P., Richmond, J. E., Hadwiger, G., Weimer, R. M., Jorgensen, E. M., and Nonet, M. L. (2001) A post-docking role for active zone protein Rim. *Nat. Neurosci.* **4,** 997–1005
47. Deng, L., Kaeser, P. S., Xu, W., and Südhof, T. C. (2011) RIM proteins activate vesicle priming by reversing autoinhibitory homodimerization of Munc13. *Neuron* **69,** 317–331
48. Han, Y., Kaeser, P. S., Südhof, T. C., and Schneggenburger, R. (2011) RIM determines Ca^{2+} channel density and vesicle docking at the presynaptic active zone. *Neuron* **69,** 304–316
49. Castillo, P. E., Schoch, S., Schmitz, F., Südhof, T. C., and Malenka, R. C. (2002) RIM1α is required for presynaptic long-term potentiation. *Nature* **415,** 327–330
50. Takada, Y., Hirano, M., Kiyonaka, S., Ueda, Y., Yamaguchi, K., Nakahara, K., Mori, M. X., and Mori, Y. (2015) Rab3 interacting molecule 3 mutations associated with autism alter regulation of voltage-dependent Ca^{2+} channels. *Cell Calcium* **58,** 296–306
51. Miki, T., Kiyonaka, S., Uriu, Y., De Waard, M., Wakamori, M., Beedle, A. M., Campbell, K. P., and Mori, Y. (2007) Mutation associated with an autosomal dominant cone-rod dystrophy CORD7 modifies RIM1-mediated modulation of voltage-dependent Ca^{2+} channels. *Channels* **1,** 144–147
52. Gandini, M. A., Sandoval, A., González-Ramírez, R., Mori, Y., de Waard, M., and Felix, R. (2011) Functional coupling of Rab3-interacting molecule 1 (RIM1) and L-type Ca^{2+} channels in insulin release. *J. Biol. Chem.* **286,** 15757–15765
53. Soong, T. W., DeMaria, C. D., Alvania, R. S., Zweifel, L. S., Liang, M. C., Mittman, S., Agnew, W. S., and Yue, D. T. (2002) Systematic identification of splice variants in human P/Q-type channel $\alpha_1$2.1 subunits: implications for current density and Ca^{2+}-dependent inactivation. *J. Neurosci.* **22,** 10142–10152
54. Giunti, P., Mantuano, E., Frontali, M., and Veneziano, L. (2015) Molecular mechanism of Spinocerebellar ataxia type 6: glutamine repeat disorder, channelopathy and transcriptional dysregulation. The multifaceted aspects of a single mutation. *Front. Cell. Neurosci.* **9,** 36
55. Aravind, L., and Landsman, D. (1998) AT-hook motifs identified in a wide variety of DNA-binding proteins. *Nucleic Acids Res.* **26,** 4413–4421
56. Maximov, A., Südhof, T. C., and Bezprozvanny, I. (1999) Association of neuronal calcium channels with modular adaptor proteins. *J. Biol. Chem.* **274,** 24453–24456
57. Wong, F. K., Nath, A. R., Chen, R. H., Gardezi, S. R., Li, Q., and Stanley, E. F. (2014) Synaptic vesicle tethering and the $Ca_V2.2$ distal C-terminal. *Front. Cell. Neurosci.* **8,** 71
58. Lipscombe, D., Pan, J. Q., and Gray, A. C. (2002) Functional diversity in neuronal voltage-gated calcium channels by alternative splicing of Ca_Va_1. *Mol. Neurobiol.* **26,** 21–44
59. Schoch, S., Mittelstaedt, T., Kaeser, P. S., Padgett, D., Feldmann, N., Chevaleyre, V., Castillo, P. E., Hammer, R. E., Han, W., Schmitz, F., Lin, W., and Südhof, T. C. (2006) Redundant functions of RIM1α and RIM2α in Ca^{2+}-triggered neurotransmitter release. *EMBO J.* **25,** 5852–5863
60. Ludwig, A., Flockerzi, V., and Hofmann, F. (1997) Regional expression and cellular localization of the α_1 and β subunit of high voltage-activated calcium channels in rat brain. *J. Neurosci.* **17,** 1339–1349
61. Burgess, D. L., Biddlecome, G. H., McDonough, S. I., Diaz, M. E., Zilinski, C. A., Bean, B. P., Campbell, K. P., and Noebels, J. L. (1999) β subunit reshuffling modifies N- and P/Q-type Ca^{2+} channel subunit compositions in lethargic mouse brain. *Mol. Cell. Neurosci.* **13,** 293–311
62. Burgess, D. L., Jones, J. M., Meisler, M. H., and Noebels, J. L. (1997) Mutation of the Ca^{2+} channel β subunit gene Cchb4 is associated with ataxia and seizures in the lethargic (lh) mouse. *Cell* **88,** 385–392
63. Chaudhuri, D., Chang, S. Y., DeMaria, C. D., Alvania, R. S., Soong, T. W., and Yue, D. T. (2004) Alternative splicing as a molecular switch for Ca^{2+}/calmodulin-dependent facilitation of P/Q-type Ca^{2+} channels. *J. Neurosci.* **24,** 6334–6342
64. Adams, P. J., Garcia, E., David, L. S., Mulatz, K. J., Spacey, S. D., and Snutch, T. P. (2009) $Ca_V2.1$ P/Q-type calcium channel alternative splicing affects

the functional impact of familial hemiplegic migraine mutations: implications for calcium channelopathies. *Channels* **3,** 110–121
65. Patil, P. G., Brody, D. L., and Yue, D. T. (1998) Preferential closed-state inactivation of neuronal calcium channels. *Neuron* **20,** 1027–1038
66. Matsuyama, Z., Kawakami, H., Maruyama, H., Izumi, Y., Komure, O., Udaka, F., Kameyama, M., Nishio, T., Kuroda, Y., Nishimura, M., and Nakamura, S. (1997) Molecular features of the CAG repeats of spinocerebellar ataxia 6 (SCA6). *Hum. Mol. Genet.* **6,** 1283–1287
67. Matsuyama, Z., Wakamori, M., Mori, Y., Kawakami, H., Nakamura, S., and Imoto, K. (1999) Direct alteration of the P/Q-type Ca^{2+} channel property by polyglutamine expansion in spinocerebellar ataxia 6. *J. Neurosci.* **19,** RC14
68. Chen, H., and Piedras-Rentería, E. S. (2007) Altered frequency-dependent inactivation and steady-state inactivation of polyglutamine-expanded α_{1A} in SCA6. *Am. J. Physiol. Cell Physiol.* **292,** C1078–C1086
69. Catterall, W. A. (2011) Voltage-gated calcium channels. *Cold Spring Harb. Perspect. Biol.* **3,** a003947
70. Wu, L. G., and Saggau, P. (1997) Presynaptic inhibition of elicited neurotransmitter release. *Trends Neurosci.* **20,** 204–212
71. Ricoy, U. M., and Frerking, M. E. (2014) Distinct roles for $Ca_V2.1$–2.3 in activity-dependent synaptic dynamics. *J. Neurophysiol.* **111,** 2404–2413
72. Müller, C. S., Haupt, A., Bildl, W., Schindler, J., Knaus, H. G., Meissner, M., Rammner, B., Striessnig, J., Flockerzi, V., Fakler, B., and Schulte, U. (2010) Quantitative proteomics of the Cav2 channel nano-environments in the mammalian brain. *Proc. Natl. Acad. Sci. U.S.A.* **107,** 14950–14957
73. Kim, J. H., and Huganir, R. L. (1999) Organization and regulation of proteins at synapses. *Curr. Opin. Cell Biol.* **11,** 248–254
74. Hering, S., Berjukow, S., Sokolov, S., Marksteiner, R., Weiss, R. G., Kraus, R., and Timin, E. N. (2000) Molecular determinants of inactivation in voltage-gated Ca^{2+} channels. *J. Physiol.* **528,** 237–249
75. Oz, S., Tsemakhovich, V., Christel, C. J., Lee, A., and Dascal, N. (2011) CaBP1 regulates voltage-dependent inactivation and activation of $Ca_V1.2$ (L-type) calcium channels. *J. Biol. Chem.* **286,** 13945–13953
76. Stotz, S. C., Jarvis, S. E., and Zamponi, G. W. (2004) Functional roles of cytoplasmic loops and pore lining transmembrane helices in the voltage-dependent inactivation of HVA calcium channels. *J. Physiol.* **554,** 263–273
77. Babich, O., Matveev, V., Harris, A. L., and Shirokov, R. (2007) Ca^{2+}-dependent inactivation of $Ca_V1.2$ channels prevents Gd^{3+} block: does Ca^{2+} block the pore of inactivated channels? *J. Gen. Physiol.* **129,** 477–483
78. Sokolov, S., Weiss, R. G., Timin, E. N., and Hering, S. (2000) Modulation of slow inactivation in class A Ca^{2+} channels by β-subunits. *J. Physiol.* **527,** 445–454
79. Craig, A. M., and Boudin, H. (2001) Molecular heterogeneity of central synapses: afferent and target regulation. *Nat. Neurosci.* **4,** 569–578
80. Ellis, J. D., Barrios-Rodiles, M., Colak, R., Irimia, M., Kim, T., Calarco, J. A., Wang, X., Pan, Q., O'Hanlon, D., Kim, P. M., Wrana, J. L., and Blencowe, B. J. (2012) Tissue-specific alternative splicing remodels protein-protein interaction networks. *Mol. Cell* **46,** 884–892
81. Liu, K. S., Siebert, M., Mertel, S., Knoche, E., Wegener, S., Wichmann, C., Matkovic, T., Muhammad, K., Depner, H., Mettke, C., Bückers, J., Hell, S. W., Müller, M., Davis, G. W., Schmitz, D., and Sigrist, S. J. (2011) RIM-binding protein, a central part of the active zone, is essential for neurotransmitter release. *Science* **334,** 1565–1569
82. Chen, J., Billings, S. E., and Nishimune, H. (2011) Calcium channels link the muscle-derived synapse organizer laminin β2 to Bassoon and CAST/Erc2 to organize presynaptic active zones. *J. Neurosci.* **31,** 512–525
83. Nishimune, H., Numata, T., Chen, J., Aoki, Y., Wang, Y., Starr, M. P., Mori, Y., and Stanford, J. A. (2012) Active zone protein Bassoon co-localizes with presynaptic calcium channel, modifies channel function, and recovers from aging related loss by exercise. *PLoS One* **7,** e38029
84. tom Dieck, S., Sanmartí-Vila, L., Langnaese, K., Richter, K., Kindler, S., Soyke, A., Wex, H., Smalla, K. H., Kämpf, U., Fränzer, J. T., Stumm, M., Garner, C. C., and Gundelfinger, E. D. (1998) Bassoon, a novel zinc-finger CAG/glutamine-repeat protein selectively localized at the active zone of presynaptic nerve terminals. *J. Cell Biol.* **142,** 499–509
85. Walker, D., Bichet, D., Campbell, K. P., and De Waard, M. (1998) A β_4 isoform-specific interaction site in the carboxyl-terminal region of the voltage-dependent Ca^{2+} channel α_{1A} subunit. *J. Biol. Chem.* **273,** 2361–2367
86. Hu, Q., Saegusa, H., Hayashi, Y., and Tanabe, T. (2005) The carboxy-terminal tail region of human Cav2.1 (P/Q-type) channel is not an essential determinant for its subcellular localization in cultured neurones. *Genes Cells* **10,** 87–96
87. Tsunemi, T., Ishikawa, K., Jin, H., and Mizusawa, H. (2008) Cell-type-specific alternative splicing in spinocerebellar ataxia type 6. *Neurosci. Lett.* **447,** 78–81
88. Sutton, K. G., McRory, J. E., Guthrie, H., Murphy, T. H., and Snutch, T. P. (1999) P/Q-type calcium channels mediate the activity-dependent feedback of syntaxin-1A. *Nature* **401,** 800–804
89. Soong, T. W., Stea, A., Hodson, C. D., Dubel, S. J., Vincent, S. R., and Snutch, T. P. (1993) Structure and functional expression of a member of the low voltage-activated calcium channel family. *Science* **260,** 1133–1136
90. Nakao, A., Miki, T., Shimono, K., Oka, H., Numata, T., Kiyonaka, S., Matsushita, K., Ogura, H., Niidome, T., Noebels, J. L., Wakamori, M., Imoto, K., and Mori, Y. (2015) Compromised maturation of GABAergic inhibition underlies abnormal network activity in the hippocampus of epileptic Ca^{2+} channel mutant mice, tottering. *Pflugers Arch.* **467,** 737–752
91. Gutnick, M. J., Lux, H. D., Swandulla, D., and Zucker, H. (1989) Voltage-dependent and calcium-dependent inactivation of calcium channel current in identified snail neurones. *J. Physiol.* **412,** 197–220
92. Lin, D. T., Makino, Y., Sharma, K., Hayashi, T., Neve, R., Takamiya, K., and Huganir, R. L. (2009) Regulation of AMPA receptor extrasynaptic insertion by 4.1N, phosphorylation and palmitoylation. *Nat. Neurosci.* **12,** 879–887